Title

Bruce suppresses autophagy-regulated caspase activity and wing tissue growth in *Drosophila*

Authors

Natsuki Shinoda[a,1], Yutaro Hama[b], Nozomi Hanawa[a] and Masayuki Miura[a,c,1]

Affiliations & Footnotes

[a]Department of Genetics, Graduate School of Pharmaceutical Sciences, The University of Tokyo, 7-3-1 Hongo, Bunkyo-ku, Tokyo 113-0033, Japan

[b]Institute for Genetic Medicine, Hokkaido University, Kita 15, Nishi 7, Kita-ku, Sapporo, Hokkaido, 060-0815, Japan

[c]Laboratory for Cell Vigor Regulation, National Institute for Basic Biology, Nishigonaka 38, Myodaiji, Okazaki, Aichi 444-8585, Japan

[1]Corresponding authors

Corresponding Authors

Natsuki Shinoda: Department of Genetics, Graduate School of Pharmaceutical Sciences, University of Tokyo 7-3-1 Hongo, Bunkyo-ku, Tokyo 113-0033, Japan. Telephone: +81-3-5841-4863. E-mail: f-shinoda.natsuki@g.ecc.u-tokyo.ac.jp

Masayuki Miura: Laboratory for Cell Vigor Regulation, National Institute for Basic Biology, Nishigonaka 38, Myodaiji, Okazaki, Aichi 444-8585, Japan. Telephone: +81-564-55-7650. E-mail: miura@nibb.ac.jp

Abstract

Caspases are cysteine-aspartic proteases that mediate both lethal and non-lethal cellular outcomes, including the promotion of tissue growth. However, the mechanisms underlying the differential regulation of these activities remain unclear. We have previously shown that among the two *Drosophila* executioner caspases, Dcp-1 and Drice, Dcp-1 promotes tissue growth in a non-lethal manner, independent of canonical apoptotic signaling. Herein, we demonstrated that overexpressed Dcp-1, but not Drice, was activated without canonical apoptosome components. TurboID-based proximity labeling revealed distinct proximal proteomes, among which Sirtuin 1, an Atg8a deacetylase, which promotes autophagy, was specifically required for Dcp-1 activation. Autophagy-related genes, including Bcl-2 family members *Debcl* and *Buffy*, are required for Dcp-1 activation. Structure-based prediction using AlphaFold3 further identified Bruce, an autophagy-regulated inhibitor of apoptosis, as a Dcp-1-specific regulator acting outside the apoptosome-mediated pathway. Physiologically, Bruce suppresses wing tissue growth. These findings indicate that non-lethal Dcp-1 activity is governed by the autophagy-Bruce axis, enabling distinct non-lethal functions independent of cell death.

Introduction

Caspases are cysteine-aspartic acid proteases that serve as the central executioners of apoptosis. In *Drosophila*, core caspase-mediated signaling for apoptosis is well conserved (Nakajima and Kuranaga, 2017; Shinoda and Miura, 2024). Upon apoptotic stimulation, the pro-apoptotic genes *rpr*, *hid*, and *grim* (*RHG*), which antagonize DIAP-1, an inhibitor of apoptosis protein (IAP), are transcriptionally upregulated. The degradation of DIAP-1 allows the initiator caspase Dronc and its activator Dark to assemble into the apoptosome, thereby triggering a proteolytic cascade that activates the executioner caspases Dcp-1 and Drice, ultimately leading to apoptosis. In addition to their role in apoptosis, caspases perform diverse non-cell death functions collectively termed caspase-dependent non-lethal cellular processes (Aram et al., 2017). However, the mechanisms that differentially regulate lethal and non-lethal caspase activity remain largely unknown.

Functional specificity appears to arise at the level of the executioner caspases. Of the two executioner caspases in *Drosophila*, Drice is more potent than Dcp-1 in inducing cell death in wing imaginal discs (Florentin and Arama, 2012). In contrast, Dcp-1 is required for autophagy triggered by starvation or proteasome dysfunction in the ovaries (Choutka et al., 2017; DeVorkin et al., 2014; Hou et al., 2008). We have previously demonstrated that Dcp-1, but not Drice, specifically promotes imaginal tissue growth independent of apoptosome and cell death (Shinoda et al., 2019). Mechanistically, we showed that cleavage-mediated inactivation of Acinus, a positive regulator of autophagy (Haberman et al., 2010; Nandi et al., 2014), which limits tissue growth independently of autophagy (Tyra et al., 2020), partly promotes tissue growth (Shinoda et al., 2019). However, the upstream regulatory mechanisms that selectively regulate Dcp-1 activity remain unknown.

Proximity labeling has emerged as a powerful approach for comprehensively analyzing molecular interactions, including protein-protein interactions (Qin et al., 2021). TurboID

enables the rapid biotinylation of lysine residues on neighboring proteins within 10 minutes in cultured cells (Branon et al., 2018). Streptavidin-based enrichment of these biotinylated proteins, followed by mass spectrometry, allows the proteome-wide identification of proteins near a target of interest. We previously generated *Drosophila* lines in which TurboID was knocked in at the C-termini of Dronc, Dcp-1, or Drice (Shinoda et al., 2019). In wing imaginal discs, TurboID-based labeling has revealed distinct proximity patterns for Dcp-1 and Drice, suggesting that each executioner caspase is associated with a unique set of neighboring proteins (Shinoda et al., 2019). We have shown that the differences in substrate specificity between Dcp-1 and Drice were consistent with their distinct proximity profiles in the ovary, as exemplified by BubR1 (Shinoda et al., 2023). Moreover, overexpression of *Fasciclin 3*, a Drice-proximal protein identified in adult brains, induces non-lethal caspase activation in a Dronc-dependent manner (Muramoto et al., 2025). These findings indicate that caspase-proximal proteins can function not only as potential substrates but also as regulatory factors.

In this study, we investigated the regulatory mechanisms underlying Dcp-1 activation. We found that the overexpression of *Dcp-1* induced a wingless phenotype. Using this phenotype as a functional readout, we found that Dcp-1 activation specifically requires its proximal protein Sirtuin 1 (Sirt1), Bcl-2 family members Debcl and Buffy, and components of the autophagy pathway. Notably, the autophagy-regulated giant IAP Bruce specifically interacts with and regulates Dcp-1 activity without affecting apoptosome-mediated core apoptotic signaling, thereby suppressing wing imaginal tissue growth. Together, these findings reveal that Bruce acts upstream to diverge the regulatory pathways of Dcp-1 and Drice, enabling Dcp-1 to mediate distinct non-lethal functions through autophagy, independent of cell death.

88 **Results**

89 ***Overexpression of Dcp-1, but not Drice, induces apoptosis***

90 Structurally, the executioner caspases, Dcp-1 and Drice, are similar, each comprising catalytic
91 P20 and P10 domains and a highly disordered N-terminal prodomain (Figure 1A). First, we
92 assessed the ability of two executioner caspases to trigger apoptosis. Using the *WP-Gal4* driver,
93 which is expressed in the wing pouch region of the wing imaginal disc (Obata et al., 2014),
94 overexpression of *Dcp-1* resulted in a wingless phenotype whereas the overexpression of *Drice*
95 did not (Figure 1B). In wing imaginal discs, *Dcp-1* overexpression induces nuclear
96 condensation (Figure 1C), indicative of apoptotic cell death. These results suggest that *Dcp-1*
97 overexpression is sufficient to induce apoptosis, consistent with our previous observations in
98 olfactory receptor neurons (Muramoto et al., 2025). Next, we examined the apoptotic potential
99 of fluorescently tagged caspases in *Drosophila* S2 cells expressing mNeonGreen (mNG)-fused
100 Dcp-1 or Drice. Dcp-1 expression caused a marked reduction in mNG intensity (Figure 1–figure
101 supplement 1A–C) and a decreased number of mNG-positive cells (Figure 1–figure supplement
102 1A, D). These effects required Dcp-1 catalytic activity, as the mutation of the catalytic cysteine
103 to glycine restored both mNG intensity and cell number (Figure 1–figure supplement 1A–D).
104 In contrast, Drice expression neither reduced mNG intensity nor decreased the number of mNG-
105 positive cells, resembling the catalytically inactive mutant (Figure 1–figure supplement 1A–D).
106 Taken together, these results demonstrate that Dcp-1, but not Drice, is activated upon
107 overexpression and induces apoptosis in multiple cell types.

108

109 ***Dcp-1 activation is independent of the apoptosome composed of Dronc and Dark***

110 Executioner caspases are typically activated by cleavage mediated by the initiator caspase,
111 Dronc, which is activated through the assembly of the Dark-dependent apoptosome (Figure 1D)
112 (Nakajima and Kuranaga, 2017; Shinoda and Miura, 2024). We previously proposed that Dcp-

113 1 can be activated independently of Dark and Dronc (Shinoda et al., 2019). To test this
114 hypothesis further, we analyzed genetic modifiers of the Dcp-1-induced wingless phenotype.
115 A heterozygous mutation in the *H99* deficiency, which encompasses the pro-apoptotic *reaper*,
116 *hid*, and *grim* (*RHG*) genes, rescued the wingless phenotype caused by *Dcp-1* overexpression
117 (Figure 1E, G). Similarly, expression of the caspase inhibitor *p35* or knockdown of *RHG* genes
118 also rescued this phenotype (Figure 1F, G), suggesting that Dcp-1 induces apoptosis in a
119 catalytic activity-dependent manner under the control of RHG proteins. In contrast, knockdown
120 of other core apoptotic components, including *Dark*, *Dronc*, and *Drice*, or overexpression of
121 the *dominant-negative form of Dronc* ($Dronc^{DN}$) failed to suppress the wingless phenotype
122 (Figure 1F, G). These findings support our earlier observation that Dcp-1 can be activated
123 independent of the canonical apoptosome composed of Dronc and Dark to mediate non-lethal
124 functions (Shinoda et al., 2019). Collectively, these results indicate that, at least under
125 overexpression conditions, Dcp-1 activation proceeds independently of the apoptosome, in
126 contrast to that of Drice.
127
128 ***Dcp-1 and Drice show distinct expression patterns among tissues***
129 Proximal proteins of caspases have emerged as potential regulators of executioner caspase
130 activity (Muramoto et al., 2025). We have previously demonstrated that the proximal protein
131 patterns of Dcp-1 and Drice differ even within the same tissue, such as wing imaginal discs
132 (Shinoda et al., 2019). Based on this, we sought to identify Dcp-1-specific regulatory factors
133 among its proximal proteins. First, we examined the tissue distribution of *Drosophila* caspases
134 using previously established *Caspase::V5::TurboID* knock-in fly lines (Shinoda et al., 2019).
135 Expression patterns were analyzed in larval tissues, including the salivary glands, fat bodies,
136 and brain (Figure 2–figure supplement 1A), with confirmed expression in wing imaginal discs
137 (Figure 2A) as well as in adult tissues, including the thorax, ovary, and testis (Figure 2–figure

138 supplement 1B). Drice was ubiquitously expressed in all examined tissues. In contrast, Dcp-1
139 expression was restricted to the larval brain, imaginal discs and adult ovaries and testes.
140
141 ***Drosophila executioner caspases associate with distinct sets of proximal proteins***
142 Next, we compared the proximal protein profiles of *Drosophila* executioner caspases, based on
143 our previous observation that Dcp-1 and Drice are associated with distinct sets of proximal
144 proteins, potentially reflecting differences in their activation mechanisms (Shinoda et al., 2019).
145 Streptavidin staining, used to visualize proteins biotinylated via TurboID-mediated proximity
146 labeling, revealed distinct patterns of Dcp-1 and Drice expression across tissues (Figure 2A,
147 Figure 2–figure supplement 1A, B). To directly compare their proximal landscapes in the same
148 cellular context, we focused on the imaginal discs. NeutrAvidin-based purification of
149 biotinylated proteins, followed by mass spectrometry, identified 818 proteins (Figure 2B, C).
150 As expected, the proximal proteomes of Dcp-1 and Drice were distinct. BubR1 and Fasciclin 3
151 isoform G, previously identified as Drice-proximal in adult brain and ovary tissues (Muramoto
152 et al., 2025; Shinoda et al., 2023), were enriched in the Drice-associated proteome (Figure 2C,
153 Table S1), suggesting that Drice maintains its proximity to specific partners across tissues.
154 Among the top Dcp-1-enriched proximal proteins was the chaperonin containing TCP1 subunit
155 8 (CCT8). To validate these findings, we generated an antibody against CCT8 (Figure 2D).
156 Western blotting confirmed the presence of CCT8 in Dcp-1::V5::TurboID samples but not in
157 Drice::V5::TurboID samples (Figure 2E). Taken together, these results show that, even when
158 expressed at comparable levels in the same tissue, Dcp-1 and Drice are associated with distinct
159 sets of proximal proteins, which is consistent with their differential regulation and functional
160 specificity.
161
162 ***Screening of Dcp-1 proximal proteins identifies Sirt1 as a Dcp-1-specific activator***

163 To identify potential regulators of Dcp-1 activation, we performed an RNAi screen targeting
164 eight genes that were selectively proximal to Dcp-1 relative to Drice and wild-type controls
165 (Dcp-1/Drice fold change > 1.5, Dcp-1/Control fold change > 10 and PSM ≧ 2; Table S1),
166 using two independent RNAi lines per gene (Figure 2F). Under normal conditions, RNAi-
167 mediated knockdown of the chaperonin components *CCT2* and *CCT8* resulted in a wingless
168 phenotype, whereas knockdown of other genes had no effect (Figure 2–figure supplement 2A).
169 Under *Dcp*-1 overexpression conditions, knockdown of *Fkbp59* or *Sirt1* partially suppressed
170 Dcp-1-induced cell death (Figure 2G, Figure 2–figure supplement 2B). The requirement for
171 Sirt1 was further confirmed using a transheteroallelic combination of two previously described
172 *Sirt1* deletion alleles, $Sirt1^{2A-7-11}$ (Furuyama et al., 2004; Xie and Golic, 2004) and $Sirt1^{4.5}$
173 (Newman et al., 2002), which significantly rescued the wingless phenotype (Figure 2H, I).
174 These results indicate that the Dcp-1-proximal protein Sirt1 is required for Dcp-1 activation
175 upon overexpression.
176
177 ***Dcp-1 activation specifically depends on Debcl, Buffy, and autophagy***
178 Sirt1, also known as dSir2, is a lysine deacetylase that promotes the expression of autophagy-
179 related genes via Atg8a deacetylation under starvation (Jacomin et al., 2020). Multiple studies
180 have linked Dcp-1 to the regulation of autophagy. Dcp-1, together with the Bcl-2 family
181 proteins Debcl and Buffy, but not Drice, has been shown to be required for starvation-induced
182 autophagy in *Drosophila* l(2)mbn cells (Hou et al., 2008), and Dcp-1 is also required for
183 autophagy in the ovary (Choutka et al., 2017; DeVorkin et al., 2014; Hou et al., 2008). More
184 recently, the BH3-only protein Sayonara (Synr) was reported to induce Dcp-1-dependent cell
185 death, which is regulated by Debcl, Buffy, and autophagy (Ikegawa et al., 2023). In contrast, a
186 gain-of-function modifier screen revealed that autophagy antagonizes Dcp-1-induced cell death

187 (Kim et al., 2010) and that Dcp-1 suppresses autophagy through cleavage-mediated inactivation
188 of Acinus (Haberman et al., 2010; Nandi et al., 2014).
189 Based on these reports, we examined whether Synr, Debcl, Buffy, and core autophagy
190 components regulate Dcp-1 activation. Knockdown of *Synr* did not suppress Dcp-1-induced
191 cell death, whereas knockdown of *Debcl* or *Buffy* significantly rescued this wingless phenotype
192 (Figure 3A, B). Similarly, knockdown of the autophagy-related genes *Atg2* and *Atg8a*
193 suppressed Dcp-1-induced cell death (Figure 3A, B), indicating that Debcl, Buffy, and
194 autophagy are required for Dcp-1 activation. To assess the specificity of these regulators, we
195 analyzed the eye ablation phenotype caused by overexpression of *Hid*, which triggers apoptosis
196 via canonical apoptotic signaling. As expected, this phenotype was rescued by *p35* expression
197 or knockdown of *RHG* genes and partially suppressed by inhibition of the Dark-, Dronc-, and
198 Drice-dependent apoptosome pathways (Figure 3C), confirming its dependence on canonical
199 apoptosis (Figure 1C). In contrast, *Hid*-induced apoptosis was not rescued by RNAi against
200 *Dcp-1* (Figure 3C), nor by knockdown of *Sirt1* or *Fkbp59* (Figure 3D). Furthermore,
201 knockdown of *Debcl*, *Buffy*, and autophagy genes failed to rescue *Hid*-induced apoptosis
202 (Figure 3E). Taken together, these results indicate that Sirt1, Debcl, Buffy, and autophagy
203 components are not general regulators of apoptosis but function as specific activators of Dcp-
204 1.
205
206 ***Cleaved Dcp-1 specifically interacts with a giant-IAP Bruce***
207 Next, we examined the molecular link between autophagy and Dcp-1 activation. Caspase
208 activation is negatively regulated by IAPs. In *Drosophila*, DIAP1 suppresses caspase activity
209 through ubiquitination (Ditzel et al., 2008) (Figure 1D). In addition to DIAP1, *Drosophila* has
210 another giant IAP, *Bruce*, which is degraded via autophagy during oogenesis (Nezis et al., 2010).
211 Bruce inhibits autophagy under nutrient-rich conditions (Hou et al., 2008), suggesting mutual

212 negative regulation of Bruce and autophagy. Bruce selectively inhibits *reaper*-induced cell
213 death, but not *hid*-induced apoptosis, suggesting a degree of pathway specificity (Domingues
214 and Ryoo, 2012). These observations led us to focus on Bruce as a potential selective regulator
215 of Dcp-1 activation.

216 The structure of human Bruce/BIRC6 has recently been resolved using cryo-electron
217 microscopy (Dietz et al., 2023; Ehrmann et al., 2023; Hunkeler et al., 2023; Liu et al., 2024),
218 revealing several conserved domains: linker domain (LD), baculoviral IAP repeat (BIR), WD40,
219 β-X1, β-X2, carbohydrate-binding module (CBM), ubiquitin-like (UBL), and ubiquitin-
220 conjugating (UBC) (Figure 4A). Human Bruce/BIRC6 ubiquitinates the activated executioner
221 caspases caspase-3 and caspase-7, but not their non-processed proforms *in vitro* (Dietz et al.,
222 2023). The BIR domain mediates interactions with ubiquitination substrates by recognizing N-
223 terminal IAP-binding motifs (IBMs) (Berthelet and Dubrez, 2013). The consensus IBM
224 sequence is defined as A(K/T/V/I)(P/A/E)(F/E/I/S/Y) (Vaux and Silke, 2005). We identified
225 IBM-like sequences at the N-termini of the P20 domains of both Dcp-1 and Drice (Figure 4B,
226 C). To assess the potential interaction between Bruce and these caspases, we used AlphaFold3
227 to predict the structure of the complexes between Bruce and the IBM-like motifs of Dcp-1 and
228 Drice (Abramson et al., 2024). Consistent with the known architecture of BIRC6, AlphaFold3
229 predicted that the BIR domain of Bruce interacts with LD, WD40, β-X1, and β-X2 domains
230 (Figure 4–figure supplement 1A, B). For structural prediction, we used a Bruce fragment
231 spanning residues 1–1960, including the BIR domain and its associated Zn^{2+}-binding site
232 (Figure 4A), and 15-residue peptides from the Dcp-1 and Drice cleavage sites encompassing
233 their IBM-like motifs (Figure 4B, C). The predicted structures revealed a high-confidence
234 interaction between Dcp-1 and the Bruce BIR domain. All five AlphaFold3 models showed
235 confident pLDDT scores (70–90) for the N-terminal residues of Dcp-1, corresponding to the
236 IBM-like motif (Figure 4D, F). The predicted binding mode resembled the canonical BIR-IBM

237 interaction observed in XIAP BIR3-Smac (Wu et al., 2000) (Figure 4–figure supplement 1C).
238 In contrast, although Drice appeared to bind to Bruce in the predicted models, the pLDDT
239 scores were consistently low (<70) across the interaction interface, including the four N-
240 terminal residues, indicating low confidence in the predicted interaction (Figure 4E, G).

241 To validate these predictions, we performed co-immunoprecipitation assays on
242 *Drosophila* S2 cells. We found that only the cleaved form of Dcp-1, which forms a head-to-tail
243 dimer composed of the P20 and P10 domains (Julien and Wells, 2017), and not the full-length
244 protein, interacted with the N-terminal BIR domain of Bruce following apoptosis induction
245 (Figure 4H), consistent with the observation that human Bruce/BIRC6 only targets cleaved
246 executioner caspases for ubiquitination *in vitro* (Dietz et al., 2023). Conversely, neither the
247 cleaved nor full-length forms of Drice showed detectable interactions with the Bruce BIR
248 domain (Figure 4H), corroborating the AlphaFold3 predictions. Taken together, these findings
249 suggest that Bruce specifically suppresses activated Dcp-1 but not Drice and serves as a
250 branching point for a Dcp-1-specific, non-canonical regulatory pathway.

251

252 ***Bruce is ubiquitously expressed in wing imaginal discs***

253 Bruce has been reported to function in oogenesis and spermatogenesis in the ovaries and testes,
254 respectively (Arama et al., 2007, 2003; Hou et al., 2008; Kaplan et al., 2010; Nezis et al., 2010).
255 However, its expression in other tissues has not been thoroughly characterized. To examine the
256 tissue distribution of Bruce, we generated CRISPR/Cas9-mediated knock-in flies in which an
257 mStayGold::C4 linker::V5-tag (Ando et al., 2024) was inserted into the N-terminus of Bruce
258 (Figure 5–figure supplement 1A). Using the knocked-in line, we confirmed that Bruce was
259 expressed in the ovaries (Figure 5–figure supplement 1B) and testes (Figure 5–figure
260 supplement 1C), consistent with previous reports (Arama et al., 2007, 2003; Hou et al., 2008;
261 Kaplan et al., 2010; Nezis et al., 2010). Western blot analysis revealed Bruce expression in both

262 adult males and females (Figure 5–figure supplement 1D). We also detected Bruce expression
263 in wing imaginal discs (Figure 5–figure supplement 1E). This signal was abolished by the
264 RNAi-mediated knockdown of *Bruce*, confirming the specificity of the signal (Figure 5–figure
265 supplement 1F). These findings indicate that Bruce not only functions in the gonads but can
266 also exert Dcp-1 regulatory functions in wing imaginal discs.
267
268 ***Bruce specifically suppresses Dcp-1 overexpression-induced cell death***
269 Next, we investigated whether Bruce regulated Dcp-1 activity. Upon overexpression of *Bruce*
270 (Figure 5A), we observed marked suppression of Dcp-1-induced cell death (Figure 5B, C).
271 Although *DIAP1* overexpression also inhibited Dcp-1 activation, this suppressive effect was
272 stronger following *Bruce* overexpression (Figure 5B, C). We examined the specificity of Bruce
273 in the regulation of other forms of cell death. As mentioned earlier, the BH3-only protein Synr
274 induces Debcl/Buffy, autophagy and Dcp-1-dependent cell death (Ikegawa et al., 2023). To
275 investigate whether Bruce was involved in Debcl/Buffy-autophagy-Dcp-1-mediated cell death,
276 we examined the role of Bruce in Synr-induced cell death. Overexpression of *Bruce*, but not
277 *DIAP1*, specifically suppressed Synr-induced cell death (Figure 5D). In contrast, *Bruce*
278 overexpression failed to rescue the eye ablation phenotype independent of autophagy caused
279 by *Hid* overexpression, whereas DIAP1 fully rescued this phenotype (Figure 5E). Taken
280 together, these results suggest that Bruce and DIAP1 regulate distinct cell death pathways, with
281 Bruce acting as a selective inhibitor of autophagy-regulated Dcp-1- and Synr-dependent cell
282 death.
283
284 ***Bruce suppresses wing tissue growth***
285 We have previously reported that Dcp-1 activity can promote imaginal tissue growth
286 independent of the core apoptosis signaling pathway, including Dronc (Shinoda et al., 2019).

287 To investigate the role of Bruce in imaginal tissue growth, we analyzed its effect on wing
288 imaginal discs using *WP-Gal4*, which drives expression throughout the wing pouch.
289 Overexpression of *p35* suppressed wing tissue growth (Figure 5F, G), whereas inhibition of
290 canonical apoptotic signaling by $Dronc^{DN}$ and *DIAP1* had no effect (Figure 5F, G). In contrast,
291 *Bruce* overexpression suppressed wing growth to an extent similar to *p35* overexpression,
292 whereas *Bruce* knockdown tended to increase wing size, although the difference was not
293 statistically significant (Figure 5F, G). We confirmed these results using *Engrailed-Gal4*, which
294 is expressed in the posterior compartment of the wing imaginal disc. *p35* overexpression
295 suppressed wing tissue growth (Figure 5H, I). In this context, the inhibition of canonical
296 apoptosis signaling by $Dronc^{DN}$ and *DIAP1* had a minor but negative effect on wing size (Figure
297 5H, I). *Bruce* overexpression suppressed wing growth, whereas *Bruce* knockdown increased
298 wing size (Figure 5H, I), indicating that Bruce negatively regulates wing tissue growth. Finally,
299 to enhance the sensitivity of the assay, we overexpressed the dominant-negative form of the
300 insulin receptor (InR^{DN}) using *WP-Gal4*, which significantly reduced wing size (Figure 5J, K).
301 Under this sensitized condition, simultaneous *Bruce* knockdown significantly enhanced wing
302 tissue growth (Figure 5J, K). Overall, these results indicate that Bruce suppresses wing tissue
303 growth.
304

305 **Discussion**

306 ***Autophagy-facilitated alternative caspase activation pathway***

307 In this study, we identified a distinct regulatory mechanism governing the activation of the
308 *Drosophila* executioner caspase, Dcp-1, in sharp contrast to its paralog Drice. Although both
309 caspases share structural similarities and are expressed in overlapping tissues, Dcp-1, but not
310 Drice, is activated upon overexpression in an apoptosome-independent, autophagy-regulated
311 manner. Previous studies have implicated Dcp-1 in the induction of autophagy (Choutka et al.,
312 2017; DeVorkin et al., 2014; Hou et al., 2008). Our findings extend this view by showing that
313 autophagy is required for Dcp-1 activation, suggesting a positive feedback loop between Dcp-
314 1 and autophagy during apoptosis. Although the precise downstream targets of the Bcl-2 family
315 proteins, Debcl and Buffy, remain unknown, their roles in autophagy regulation (Hou et al.,
316 2008) suggest that they influence Dcp-1 activity through autophagic pathways. Additionally,
317 we identified Bruce, a giant inhibitor of apoptotic proteins, as a Dcp-1-specific suppressor.
318 Functionally, Bruce limits wing tissue growth, suggesting that Dcp-1 activation contributes to
319 growth regulation in a non-lethal manner (Shinoda et al., 2019). Taken together, our results
320 demonstrate that the regulatory mechanisms of Dcp-1 and Drice diverge at the level of IAPs
321 and that Dcp-1 activation is regulated by autophagy, enabling specific non-lethal functions that
322 promote tissue growth independent of canonical apoptotic signaling (Figure 5L). It is important
323 to note that Dcp-1 can also suppress autophagy through cleavage of Acinus (Haberman et al.,
324 2010; Nandi et al., 2014). Although this may seem contradictory, the ability of caspases to
325 function in a non-lethal manner requires strict prevention of excessive activation. Such
326 suppression may represent a key mechanism that enables non-lethal caspase activity.

327 It is also important to understand how cells determine the usage of canonical versus
328 alternative caspase activation pathways depending on physiological or environmental
329 conditions. In mammals, two major apoptotic pathways are activated by distinct initiator

330 caspases, caspase-8 and caspase-9, in response to different upstream signals (Newton et al.,
331 2024). Similarly, in *Drosophila*, while most developmental cell death is driven by canonical
332 apoptotic signaling involving Dronc (Xu et al., 2005), alternative caspase activation pathways
333 may be preferentially engaged in response to environmental stimuli, such as starvation or heat
334 shock.
335
336 ***Initiator caspase-independent activation mechanism for Dcp-1***
337 The mechanism by which Dcp-1 is activated by itself remains an open and important question.
338 In contrast to Drice, Dcp-1 is activated upon overexpression in an apoptosome-independent but
339 autophagy-dependent manner. Unlike initiator caspases, executioner caspases such as Dcp-1
340 generally lack long N-terminal prodomains and require proteolytic cleavage to become
341 catalytically active. Proximity-labeling analysis revealed that Dcp-1 was predominantly
342 associated with the chaperonin subunit CCT8 (Figure 2E). Given that the overexpression of
343 *Dcp-1* increases its local concentration for activation, we propose that its accumulation in the
344 chaperonin complex may serve as a local scaffold for caspase activation. This model implies a
345 spatially restricted mode of regulation in which caspase activity is compartmentalized within
346 the cell. In this model, we speculated that Dcp-1 activation occurs sporadically in subcellular
347 regions enriched in activators or scaffolding molecules such as CCT8. Under these conditions,
348 Dcp-1 activation may need to be tightly regulated to prevent its unintended proteolytic activity.
349 Supporting this notion, we proposed that Bruce functions as a basal suppressor of Dcp-1 in non-
350 lethal contexts, restraining caspase activity when full apoptotic signaling is not engaged.
351
352 ***Distinct roles of evolutionarily multiplicated executioner caspases***
353 Caspases are essential cysteine proteases that execute apoptotic cell death and are conserved
354 from *C. elegans* to mammals (Shinoda and Miura, 2024). Multiple executioner caspases exist,

355 including caspase-3 and caspase-7 in mammals and Dcp-1 and Drice in *Drosophila*. Although
356 these enzymes are often functionally redundant in apoptosis, growing evidence indicates that
357 each executioner caspase harbors distinct substrate specificities and fulfills non-overlapping
358 roles (Boucher et al., 2012; Desroches and Denault, 2019; Shinoda et al., 2023, 2019; Walsh et
359 al., 2008). In mammals, caspase-3 and caspase-7 exhibit high sequence similarity but differ in
360 their substrate preferences. Caspase-7, for instance, contains polybasic residues in its exosite
361 that enhance its ability to cleave RNA-binding proteins, a function not observed in caspase-3
362 (Boucher et al., 2012). Mechanistically, this exosite enables caspase-7 to interact directly with
363 RNA, thereby promoting selective proteolysis of RNA-associated substrates (Desroches and
364 Denault, 2019). Furthermore, we have recently demonstrated that caspase-7 is essential for
365 early-peaking caspase activity at the plasma membrane during apoptosis, a process mediated
366 by its N-terminal intrinsically disordered region, which facilitates rapid efferocytosis of
367 apoptotic cells (Taira et al., 2025). In this study, we demonstrated that *Drosophila* executioner
368 caspases Dcp-1 and Drice are also subject to distinct activation mechanisms for the specific
369 non-lethal function of tissue growth. These findings underscore that the evolutionary expansion
370 of executioner caspases does not merely provide functional redundancy for apoptotic execution
371 but rather confers unique biochemical properties and regulatory roles under distinct cellular
372 contexts. This diversification allows executioner caspases to participate in both lethal and non-
373 lethal cellular processes, highlighting their broader functional repertoire beyond canonical
374 apoptosis.
375

376 **Methods**

377 ***Fly strains and rearing conditions***

378 We raised the flies in standard *Drosophila* medium at 25°C. For in vivo biotin labeling
379 experiments, flies were raised in standard *Drosophila* medium supplemented with 100 μM (+)-
380 biotin (#029-08713, WAKO). The fly strains used in this study are listed in Table S2.
381 Genotypes corresponding to each figure are shown in Table S3.

382

383 ***Intrinsically disordered region prediction***

384 Amino acid sequences were obtained from the FlyBase database [https://flybase.org/].
385 Disordered regions were predicted using the PSIPRED protein sequence analysis workbench in
386 DISOPRED3 [http://bioinf.cs.ucl.ac.uk/psipred/].

387

388 ***Adult wings and eyes phenotypes scoring***

389 Adult female flies were anesthetized using CO_2. The wing and eye images were acquired using
390 a Leica MZ16F fluorescent stereomicroscope (Leica Microsystems) equipped with a Leica
391 DFC450 C CCD camera. Each wing was manually classified into one of four categories: *Intact*
392 (no defect), *Mild* (≧50% of wing area intact), *Severe* (<50% but ≧5% of wing area intact), and
393 *Wingless* (<5% of wing area intact).

394

395 ***Molecular cloning***

396 For *pAc5-Caspases-myc-mNeonGreen*, the coding sequences of *Dcp-1* and *Drice* were
397 amplified using PCR from the corresponding *pUASz-Caspase::V5::TurboID* plasmids
398 (Muramoto et al., 2025). The coding sequence of myc-tagged mNeonGreen was PCR-amplified
399 from *pUASz-Drice::myc::mNeonGreen plasmid* (Muramoto et al., 2025). The two fragments

400 were ligated into EcoRI/XhoI-digested *pAc5_STABLE2_neo* (González et al., 2011) using In-
401 Fusion (TaKaRa, Z9648N).

402 For *pCold I-EcoRI-CCT8-EcoRI*, the coding sequence of *CCT8* was PCR-amplified
403 from *Drosophila* cDNA, and the fragment was ligated into the *Eco*RI-digested *pCold I DNA*
404 vector (#3361, TaKaRa) using In-Fusion.

405 For *pAc5-Caspases^{CG}-myc*, the coding sequences of *Dcp-1* and *Drice* were PCR
406 amplified from the corresponding *pAc5-Caspases-myc-mNeonGreen* plasmids. The fragments
407 were ligated into EcoRI/BamHI-digested *pAc5_STABLE2_neo* (González et al., 2011) using
408 In-Fusion. For pAct-Bruce$^{1\text{-}900a}$a-3xFLAG, the first 900 aa of the coding sequences of *Bruce*
409 were PCR-amplified from *Drosophila* cDNA, and the fragment was ligated into the *Eco*RI-
410 digested *pAc5-Fasciclin 3 isoform A-3xFLAG* plasmids (Muramoto et al., 2025) using In-
411 Fusion. For *pAc5-3xFLAG-mRuby*3, *Drosophila* codon-optimized mRuby3 was synthesized
412 (Integrated DNA Technologies, Coralville, IA, USA) and ligated into the BamHI-digested
413 *pAc5-3xFLAG-Bub3* plasmids (Shinoda et al., 2023) using In-Fusion.

414 For mStayGold::C4 linker::V5-tag knock-in for Bruce, the guide RNA was identified
415 using the CRISPR Optimal Target Finder tool available on flyCRISPR
416 [http://flycrispr.molbio.wisc.edu/]. The DNA fragments for the guide RNA were subcloned into
417 BbsI-digested pDCC6 vectors (#59985, Addgene) (Gokcezade et al., 2014) to establish the
418 *pDCC6-dBruce-sgRNA* plasmid. The following primers were annealed to generate the DNA
419 fragments for guide RNAs: 5′-CTTCGCTTGCTTGAGGACGCGCTGC-3′ and 5′-
420 AAACGCAGCGCGTCCTCAAGCAAGC-3′. For the generation of the homology-directed
421 repair template (*pBac-mStayGold-c4-V5-dBruce-donor-3xP3-dsRed-polyA*), DNA fragments
422 of the 5′ homology arm were assembled into the BsaI site, and the DNA fragment of the 3′
423 homology arm with mStayGold::C4 linker::V5-tag was assembled into the SapI site of
424 pBac[3xP3-DsRed_polyA_Scarless_TK] (Shinoda et al., 2019) using In-Fusion. The PAM

425 sequence (TGG) of the gRNA-binding sites in the donor template was mutated (TGA) to
426 prevent Cas9-directed cleavage following homology-directed repair. The mStayGold::C4
427 linker::V5-tag fragment was amplified from pRSETB/mStayGold(c4) (#212018; Addgene)
428 (Ando et al., 2024) with V5-tag harboring primers. DNA fragments were amplified using PCR
429 with the following primers: dBruce 5′ homology arm (forward primer, 5′-
430 TGAAGGTCTCCTTAAAAGCCCGATTGGCGGCGCAGGAAGT-3′, and reverse primer,
431 5′-TCTTTCTAGGGTTAATCGAGTGCCCAGGGGGCGCGCGAGT-3′), dBruce 3′
432 homology arm-1 (forward primer, 5′-
433 TCTTTCTAGGGTTAATTTTTGGCATTCACAGGCGATTGCT-3′, and reverse primer, 5′-
434 TCCGGAGGTGCGCCGCGGCAATTTG-3′), mStayGold-C4 linker-V5-tag (forward primer,
435 5′-CGGCGCACCTCCGGAATGGTGTCTACAGGCGAGGAGCTGT-3′, and reverse primer,
436 5′-
437 GGTGCTGTCCAGGCCCAGCAGGGGGTTGGGGATGGGCTTGCCCACGGCAGAAGC
438 AGAAGGCTCGTGC-3′), 3′ homology arm-2 with mutated PAM (forward primer, 5′-
439 GGCCTGGACAGCACCGCCACGGAGCAGCATCATCAGCAGCGCGTCCTCAA-3′, and
440 reverse primer, 5′-GACGGCTCTTCATTAACTCTTAAATCAAATTTAAATTGAA-3′). The
441 established plasmids were injected into *yw; nos-Cas9(II-attP40)* for CRISPR/Cas9-mediated
442 transgenesis (BestGene Inc.). Each DsRed-positive transformant was isogenized and confirmed
443 using genomic PCR and sequencing.
444 All established plasmids were sequenced by Eurofins, Inc. The detailed plasmid DNA
445 sequences are available upon request.
446
447 ***Cell culture***

448 *Drosophila* S2 cells were grown at 25°C in Schneider's *Drosophila* medium (GIBCO,
449 21720001) supplemented with 10% (v/v) heat-inactivated fetal bovine serum, 100 U/mL
450 penicillin, and 100 μg/mL streptomycin (WAKO, 168-23191).
451
452 ***mNeonGreen signal quantification of S2 cells***
453 *Drosophila* S2 cells (2.5×10^5) seeded in 24-well plates were transfected with 200 ng of the
454 desired plasmid using Effectene Transfection Reagent (QIAGEN, 301427) following the
455 manufacturer's protocol. Sixteen hours after transfection, cells were transferred to four-
456 compartment glass-bottomed dishes (Greiner #627870). After another 24 hours, images were
457 captured using a Leica TCS SP8 confocal microscope (Leica Microsystems).
458 The mNeon Green intensity was quantified using Fiji (ImageJ) software (NIH Image).
459 Images were analyzed automatically using the ImageJ macro, as previously described (Fujisawa
460 et al., 2020) with modifications. Briefly, the mNeonGreen channel was filtered by the
461 "Gaussian Blur (sigma = 1)", processed with "Auto Threshold ("Mean" method)," processed
462 with "Watershed," and processed with "Analyze particles (size = 40–200 μm^2, circularity =
463 0.2–1.0)" to define the region of interest. For a given region of interest, the average mNeon
464 Green intensity was measured.
465
466 ***Protein preparation of Drosophila tissues***
467 Whole larvae without digestive tract and fatobodies, larval salivary glands, fatbodies, brains,
468 wing discs and whole adults, adult thoraxes, ovaries, and testises of desired genotype were
469 dissected and lysed with RIPAi buffer (50 mM Tris-HCl, pH 8.0, 150 mM sodium chloride, 0.5
470 wt/vol% sodium deoxycholate, 0.1% w/v sodium dodecyl sulfate, and 1.0% w/v NP-40)
471 supplemented with cOmplete ULTRA EDTA-free protease inhibitor cocktail (#05892953001,
472 Roche). Samples were homogenized and centrifuged at 20,000 × *g*, 4°C for 10 min. The

473 supernatants were collected and snap-frozen in liquid nitrogen. Protein concentrations were
474 determined using the BCA assay (#297-73101, Wako) following the manufacturer's protocol.
475 The samples were mixed with Laemmli buffer, boiled at 95°C for 5 min, and then subjected to
476 western blotting analysis.
477
478 ***Western blotting***
479 Each sample was separated using SDS-PAGE. The proteins were then transferred onto
480 Immobilon-P polyvinylidene fluoride membranes (#IPVH00010; Millipore) for
481 immunoblotting. Membranes were blocked with 4% skim milk diluted in 1× TBST.
482 Immunoblotting was performed using the antibodies mentioned below, which were diluted with
483 4% skim milk. Signals were visualized using Immobilon Western Chemiluminescent HRP
484 Substrate (#WBKLS0500; Millipore) and FUSION SOLO. 7S. EDGE (Vilber-Lourmat).
485 Contrast and brightness adjustments were applied equally using Fiji (ImageJ) software (NIH
486 Image).
487 The primary antibodies used included mouse anti-V5 monoclonal antibody (1:1,000,
488 #46-0705, Invitrogen), mouse anti-FLAG M2 monoclonal antibody (1:5,000, Sigma), rabbit
489 anti-CCT8 polyclonal antibody (1:5,000, this study), rabbit anti-Myc-Tag (71D10) monoclonal
490 antibody (1:5,000, #2278, CST), rabbit anti-3xDYKDDDDK Tag (3xFLAG Tag) (E7C5T)
491 monoclonal antibody (1:5,000, #87537, CST), mouse anti-alpha tubulin (DM1A) monoclonal
492 antibody (1:10,000, #T9026, Sigma), mouse anti-Histone H3 (1B1B2) monoclonal antibody
493 (1:10,000, #14269, CST), and mouse anti-Actin monoclonal antibody (1:5,000; #A4700,
494 Sigma). The secondary antibodies used were goat anti-rabbit IgG horseradish peroxidase
495 (HRP)-conjugated antibody (1:5,000, #7074S, CST) and goat/rabbit/donkey anti-mouse IgG
496 HRP Conjugate (1:5,000, #W402B, Promega). The membranes for streptavidin blotting were

497 blocked with 3% bovine serum albumin. Streptavidin blotting was performed using
498 streptavidin-HRP (1:10,000, #SA10001; Invitrogen) diluted in 3% bovine serum albumin.
499
500 ***Experimental design for liquid chromatography–mass spectrometry (LC-MS/MS) analyses***
501 Two biological replicates were analyzed for each experimental condition to determine the
502 abundance of Drice/Dcp-1::TurboID relative to the control.
503
504 ***Purification of biotinylated proteins***
505 Samples were prepared as previously described (Shinoda et al., 2023). Briefly, 100 μg of
506 biotinylated protein-containing lysate was subjected to FG-NeutrAvidin bead (#TAS8848
507 N1171, Tamagawa Seiki) purification. FG-NeutrAvidin beads (25 μL, approximately 500 μg)
508 were washed three times with RIPA buffer. Benzonase-treated biotinylated protein samples
509 suspended in 1 mL of RIPA buffer were incubated overnight at 4°C. Conjugated beads were
510 magnetically isolated and washed with 500 μL of an ice-cold RIPA buffer solution, 1 M KCl
511 solution, 0.1 M Na_2CO_3 solution, and 4 M urea solution. For western blot analyses, the purified
512 samples were mixed with Laemmli buffer, boiled at 95°C for 5 min, and then subjected to
513 western blot analysis. For LC-MS/MS analysis, the purified samples were washed with 500 μL
514 ultrapure water (#214-01301, Wako) and 500 μL of 50 mM ammonium bicarbonate. The
515 samples were then mixed with 50 μL of 0.1% Rapigest diluted in 50 mM ammonium
516 bicarbonate, and 5 μL of 50 mM TCEP was subsequently added. Samples were incubated at
517 60°C for 5 min, and then 2.5 μL of 200 mM methyl methanethiosulfonate was added. One
518 microgram sequence-grade modified trypsin (#V5111, Promega) was then added for on-bead
519 trypsin digestion at 37°C, leaving the treatment for 16 h. The beads were then magnetically
520 isolated, and 60 μL of the supernatant was collected. Then, 3 μL of 10% trifluoroacetic acid
521 was added to the supernatants, incubating them at 37°C for 60 min with gentle agitation. The

522 samples were then centrifuged at 20,000 × *g*, 4°C for 10 min. The peptides were then
523 desalinated and purified using a GL-tip SDB (#7820-11200, GL Sciences) following the
524 manufacturer's instructions. The samples were speed-backed at 45°C for 30 min and dissolved
525 in 25 µL of 0.1% formic acid. The samples were then centrifuged at 20,000 × *g*, 4°C for 10
526 min, and the supernatants were collected. The peptide concentrations were determined using
527 the BCA assay. Finally, 500 ng of the purified protein was subjected to LC-MS/MS analysis.
528
529 ***LC-MS/MS analyses***
530 Samples were loaded onto an Acclaim PepMap 100 C18 column (75 µm x 2 cm, 3 µm particle
531 size and 100 Å pore size; #164946, Thermo Fisher Scientific) and separated on a nano-capillary
532 C18 column, (75 µm x 12.5 cm, 3 µm particle size, #NTCC-360/75-3-125, Nikkyo Technos)
533 using EASY-nLC 1200 system (Thermo Fisher Scientific). Elution conditions are listed in
534 Table S4. The separated peptides were analyzed using QExactive (Thermo Fisher Scientific) in
535 data-dependent MS/MS mode. The parameters for the MS/MS analysis are listed in Table S5.
536 The collected data were analyzed using Proteome Discoverer (PD) 2.2 software with the
537 Sequest HT search engine. The parameters for the PD 2.2 analysis are described in Table S6.
538 Peptides were filtered at a false discovery rate of 0.01 using the Percolator node. Label-free
539 quantification was performed based on the intensities of the precursor ions using a precursor-
540 ion quantifier node. Normalization was performed using the total amount of peptides in all
541 average scaling modes. MS proteomic data were deposited in the ProteomeXchange
542 Consortium via the jPOST partner repository with the dataset identifier PXD067425 (Okuda et
543 al., 2017).
544
545 ***Anti-CCT8 antibody generation***

546 CCT8 was expressed in *Escherichia coli BL21* transformed with *pCold I-EcoRI-CCT8-EcoRI*.
547 Cells were grown at 37 °C overnight, diluted to OD_{600} 0.2 and cultured until OD_{600} 0.5 at 37°C.
548 Protein expression was induced by the addition of 1 mM IPTG at 15°C for 24 h. Cells were
549 centrifuged at 4000 × *g*, 4 °C for 20 min and resuspended in phosphate-buffered saline (PBS).
550 Cells were centrifuged at 4000 × *g*, 4°C for 10 min. Purification of 6x His-tagged CCT8 was
551 performed using the QIAexpress Ni-NTA Fast Start Kit (#30600, Qiagen) according to the
552 manufacturer's protocol: purification of 6xHis-tagged proteins under denaturing conditions.
553 Briefly, the cell pellets were lysed in Lysis Buffer (Denaturing Buffer adjusted to pH 8.0) with
554 gentle agitation for 60 min. The sample was centrifuged at 9,200 × *g*, 20°C for 30 min. The
555 supernatant was applied to Fast Start column and washed twice with Wash Buffer (Denaturing
556 Buffer adjusted to pH 6.3). Proteins were eluted using Elution Buffer (Denaturing Buffer
557 adjusted to pH 4.5). Polyclonal antibodies were raised in rabbits using purified 6xHis-tagged
558 CCT8 as an immunogen (Eurofins Inc.).
559
560 ***Protein complexes prediction with AlphaFold3***
561 Amino acid sequences were obtained from the FlyBase database [https://flybase.org/]. The
562 protein complex structures were predicted using AlphaFold3 (Abramson et al., 2024) on the
563 AlphaFold server [https://alphafoldserver.com/].
564
565 ***Co-immunoprecipitation***
566 *Drosophila* S2 cells (2.0×10^6) seeded in 6-well plates were transfected with the desired
567 plasmid using Effectene Transfection Reagent. For live cell lysate, *Drosophila* S2 cells were
568 lysed on ice using 550 µL of IP lysis buffer (50 mM Tris-HCl (pH 7.5), 150 mM NaCl, 0.5%
569 NP-40) supplemented with cOmplete ULTRA EDTA-free protease inhibitor cocktail. For
570 apoptotic cell lysate, the cells were treated with 10 µg/mL cycloheximide (#C7698, Sigma) for

571 apoptosis induction. After 6 h of incubation, cells were harvested and centrifuged at 800 × *g*,
572 4 °C for 5 min and washed twice. Then, cells were lysed by using 550 μL of IP lysis buffer (50
573 mM Tris-HCl (pH 7.5), 150 mM NaCl, and 0.5% NP-40) supplemented with cOmplete
574 ULTRA EDTA-free protease inhibitor cocktail. The cell lysates were centrifuged at 20,000 × *g*,
575 4 °C for 5 min. Supernatants (50 μL) were collected as inputs. The remainder of the supernatant
576 was incubated for 2 h at 4°C with 20 μL of anti-DDDDK-tag mAb-Magnetic Agarose (#M185-
577 10R, MBL) equilibrated with the IP lysis buffer. The beads were washed thrice in IP lysis buffer
578 and boiled for 5 min at 95°C with 50 μL 1× Laemmli buffer. The samples were magnetically
579 separated, and the supernatants were subjected to SDS-PAGE.
580
581 ***Immunohistochemistry***
582 Wing imaginal discs of the late third-instar larvae and testes and ovaries of the adults were fixed
583 with 4% paraformaldehyde in PBS. The wing imaginal discs and testes samples were washed
584 in PBS containing 0.1% Triton X-100 (PBST), and the ovary samples were washed in 1.0%
585 PBST, blocked in PBST with 5% normal donkey serum (PBSTn) for 30 min, and incubated
586 with primary antibodies in PBSTn overnight at 4°C. The samples were washed with PBST,
587 incubated for 2 h with secondary antibodies suspended in PBSTn, and washed again with PBST.
588 Images were captured using a TCS SP8 microscope (Leica Microsystems).
589 The primary antibodies used were rabbit anti-HA (Y11) polyclonal antibody (1:100,
590 #sc-805, Santa Cruz), mouse anti-Myc-tag monoclonal antibody (1:500, #R950-25, Invitrogen)
591 and mouse anti-V5 tag monoclonal antibody (1:100, #960-25, Invitrogen). The secondary
592 antibodies used were Cy3-conjugated donkey anti-rabbit IgG (1:250, #711-165-152, Jackson
593 Immuno Research), Alexa488-conjugated donkey anti-mouse IgG (1:500 (Myc) or 1:100 (V5),
594 #A-21202, Thermo Fisher Scientific). Hoechst 33342 (8 μM; #H3570, Invitrogen) for nuclear
595 staining and Phalloidin-iFluor633 (1 : 1000, #ab176758, Abcam) for F-actin staining were used

596 during the secondary antibody incubation. Images were analyzed and edited using ImageJ
597 software.
598
599 ***Wing size measurement***
600 Flies were raised, and their wings were mounted and digitized as previously described (Shinoda
601 et al., 2019). Briefly, flies were placed on an acetic acid agar plate (2% agar, 1% sucrose, and
602 0.36% acetic acid) to lay eggs overnight. The plates were collected, and the eggs were incubated
603 at 25°C for 24 h. The 1st instar larvae were collected from the agar plate, and 30 larvae were
604 placed in one vial to precisely control the larval density. These flies were raised at 25°C. After
605 more than two days of hatching, the adult female flies were collected and submerged in 99.5%
606 ethanol to dehydrate for 24 hours. Dehydrated flies were dissected to mount their wings using
607 Euparal (Waldeck) with the dorsal side upward. Images were digitized using an upright
608 microscope (Leica DM5000B; Leica Microsystems) equipped with a CCD camera. The wing
609 size was measured using a Drosophila wing digital twin
610 [https://datamarkin.com/models/drosophila-wings-beta] developed by Datamarkin. Areas 0, 1,
611 and 2 were quantified as the anterior parts, whereas areas 4, 6, 7, and 8 were quantified as the
612 posterior parts, respectively.
613
614 ***Statistical analysis***
615 The data are presented as the means ± standard error of measurement (SEM). *p*-values were
616 calculated using a one-way analysis of variance (ANOVA), followed by Sidak's multiple
617 comparison test for selected pairs (Figure 1–figure supplement 1B, C, D; Figure 5K), or
618 Dunnett's multiple comparison test using GraphPad Prism 8. NS: $p \geqq 0.05$, †: $p < 0.05$.
619

620 **Acknowledgments**

621 We would like to thank G. W. Davis, R. Carthew, B. Hay, C-H. Cheng, H. Richardson, S. K.
622 Yoo, H. Steller, Y. Hiromi, H. D. Ryoo, the FlyORF Zurich ORFeome Project, Bloomington
623 *Drosophila* Stock Center, Vienna Drosophila Resource Center, Kyoto Stock Center, and NIG-
624 FLY for providing the fly strains. We thank Datamarkin for providing the Drosophila wing
625 digital twin tool. We thank Dr. S. Hirayama, Dr. S. Murata, and the One-Stop Sharing Faculty
626 Center for Future Drug Discovery at the Graduate School of Pharmaceutical Sciences,
627 University of Tokyo, for the LC-MS/MS analysis. We thank Miura's lab members for their
628 technical assistance and discussions; in particular, K. Takenaga for preparing the fly food and
629 R. Takamoto for experimental support. We thank *Editage* [www.editage.com] for the English
630 language editing of this manuscript. This work was supported by grants from the Ministry of
631 Education, Culture, Sports, Science, and Technology of Japan (KAKENHI Grant Numbers
632 19K16137, 21K15080, 22H05586, and 23K05747 to N.S. and 21H04774, 23H04766,
633 24H00567, and 25H01842 to M.M.), the Japan Agency for Medical Research and Development
634 (AMED; Grant number JP21gm5010001 to M.M.), and grants from the Takeda Science
635 Foundation and Sumitomo Foundation to N.S.

636

637 **Author Contributions**

638 N.S. and M.M. designed the study; N.S. conducted most of the experiments and analyzed most
639 of the data; Y.H conducted protein structural predictions; N.H. analyzed the expression patterns
640 of Drosophila caspases; and N.S. and M.M. wrote the manuscript.

641

642 **Conflict of Interest**

643 The authors declare that they have no conflict of interest.

644

References

Abramson J, Adler J, Dunger J, Evans R, Green T, Pritzel A, Ronneberger O, Willmore L, Ballard AJ, Bambrick J, Bodenstein SW, Evans DA, Hung C-C, O'Neill M, Reiman D, Tunyasuvunakool K, Wu Z, Žemgulytė A, Arvaniti E, Beattie C, Bertolli O, Bridgland A, Cherepanov A, Congreve M, Cowen-Rivers AI, Cowie A, Figurnov M, Fuchs FB, Gladman H, Jain R, Khan YA, Low CMR, Perlin K, Potapenko A, Savy P, Singh S, Stecula A, Thillaisundaram A, Tong C, Yakneen S, Zhong ED, Zielinski M, Žídek A, Bapst V, Kohli P, Jaderberg M, Hassabis D, Jumper JM. 2024. Accurate structure prediction of biomolecular interactions with AlphaFold 3. *Nature* **630**:493–500.

Ando R, Shimozono S, Ago H, Takagi M, Sugiyama M, Kurokawa H, Hirano M, Niino Y, Ueno G, Ishidate F, Fujiwara T, Okada Y, Yamamoto M, Miyawaki A. 2024. StayGold variants for molecular fusion and membrane-targeting applications. *Nat Methods* **21**:648–656.

Aram L, Yacobi-Sharon K, Arama E. 2017. CDPs: caspase-dependent non-lethal cellular processes. *Cell Death Differ* **24**:1307–1310.

Arama E, Agapite J, Steller H. 2003. Caspase activity and a specific cytochrome C are required for sperm differentiation in Drosophila. *Dev Cell* **4**:687–697.

Arama E, Bader M, Rieckhof GE, Steller H. 2007. A ubiquitin ligase complex regulates caspase activation during sperm differentiation in Drosophila. *PLoS Biol* **5**:e251.

Berthelet J, Dubrez L. 2013. Regulation of apoptosis by inhibitors of apoptosis (IAPs). *Cells* **2**:163–187.

Boucher D, Blais V, Denault J-B. 2012. Caspase-7 uses an exosite to promote poly(ADP ribose) polymerase 1 proteolysis. *Proc Natl Acad Sci U S A* **109**:5669–5674.

Branon TC, Bosch JA, Sanchez AD, Udeshi ND, Svinkina T, Carr SA, Feldman JL, Perrimon N, Ting AY. 2018. Efficient proximity labeling in living cells and organisms with TurboID. *Nat Biotechnol* **36**:880–887.

Choutka C, DeVorkin L, Go NE, Hou Y-CC, Moradian A, Morin GB, Gorski SM. 2017. Hsp83 loss suppresses proteasomal activity resulting in an upregulation of caspase-dependent compensatory autophagy. *Autophagy* **13**:1573–1589.

Desroches A, Denault J-B. 2019. Caspase-7 uses RNA to enhance proteolysis of poly(ADP-ribose) polymerase 1 and other RNA-binding proteins. *Proc Natl Acad Sci U S A* **116**:21521–21528.

DeVorkin L, Go NE, Hou Y-CC, Moradian A, Morin GB, Gorski SM. 2014. The Drosophila effector caspase Dcp-1 regulates mitochondrial dynamics and autophagic flux via SesB. *J Cell Biol* **205**:477–492.

Dietz L, Ellison CJ, Riechmann C, Cassidy CK, Felfoldi FD, Pinto-Fernández A, Kessler BM, Elliott PR. 2023. Structural basis for SMAC-mediated antagonism of caspase inhibition by the giant ubiquitin ligase BIRC6. *Science* **379**:1112–1117.

Ditzel M, Broemer M, Tenev T, Bolduc C, Lee TV, Rigbolt KTG, Elliott R, Zvelebil M, Blagoev B, Bergmann A, Meier P. 2008. Inactivation of effector caspases through nondegradative polyubiquitylation. *Mol Cell* **32**:540–553.

Domingues C, Ryoo HD. 2012. Drosophila BRUCE inhibits apoptosis through non-lysine ubiquitination of the IAP-antagonist REAPER. *Cell Death Differ* **19**:470–477.

Ehrmann JF, Grabarczyk DB, Heinke M, Deszcz L, Kurzbauer R, Hudecz O, Shulkina A, Gogova R, Meinhart A, Versteeg GA, Clausen T. 2023. Structural basis for regulation of apoptosis and autophagy by the BIRC6/SMAC complex. *Science* **379**:1117–1123.

Florentin A, Arama E. 2012. Caspase levels and execution efficiencies determine the apoptotic potential of the cell. *J Cell Biol* **196**:513–527.

693 Fujisawa Y, Shinoda N, Chihara T, Miura M. 2020. ROS Regulate Caspase-Dependent Cell
694 Delamination without Apoptosis in the Drosophila Pupal Notum. *iScience* **23**:101413.
695 Furuyama T, Banerjee R, Breen TR, Harte PJ. 2004. SIR2 is required for polycomb silencing
696 and is associated with an E(Z) histone methyltransferase complex. *Curr Biol* **14**:1812–
697 1821.
698 Gokcezade J, Sienski G, Duchek P. 2014. Efficient CRISPR/Cas9 plasmids for rapid and
699 versatile genome editing in Drosophila. *G3 (Bethesda)* **4**:2279–2282.
700 González M, Martín-Ruíz I, Jiménez S, Pirone L, Barrio R, Sutherland JD. 2011. Generation
701 of stable Drosophila cell lines using multicistronic vectors. *Sci Rep* **1**:75.
702 Haberman AS, Akbar MA, Ray S, Krämer H. 2010. Drosophila acinus encodes a novel
703 regulator of endocytic and autophagic trafficking. *Development* **137**:2157–2166.
704 Hou Y-CC, Chittaranjan S, Barbosa SG, McCall K, Gorski SM. 2008. Effector caspase Dcp-1
705 and IAP protein Bruce regulate starvation-induced autophagy during Drosophila
706 melanogaster oogenesis. *J Cell Biol* **182**:1127–1139.
707 Hunkeler M, Jin CY, Fischer ES. 2023. Structures of BIRC6-client complexes provide a
708 mechanism of SMAC-mediated release of caspases. *Science* **379**:1105–1111.
709 Ikegawa Y, Combet C, Groussin M, Navratil V, Safar-Remali S, Shiota T, Aouacheria A, Yoo
710 SK. 2023. Evidence for existence of an apoptosis-inducing BH3-only protein, sayonara,
711 in Drosophila. *EMBO J* **42**:e110454.
712 Jacomin A-C, Petridi S, Di Monaco M, Bhujabal Z, Jain A, Mulakkal NC, Palara A, Powell EL,
713 Chung B, Zampronio C, Jones A, Cameron A, Johansen T, Nezis IP. 2020. Regulation
714 of Expression of Autophagy Genes by Atg8a-Interacting Partners Sequoia, YL-1, and
715 Sir2 in Drosophila. *Cell Rep* **31**:107695.
716 Julien O, Wells JA. 2017. Caspases and their substrates. *Cell Death Differ* **24**:1380–1389.
717 Kaplan Y, Gibbs-Bar L, Kalifa Y, Feinstein-Rotkopf Y, Arama E. 2010. Gradients of a
718 ubiquitin E3 ligase inhibitor and a caspase inhibitor determine differentiation or death
719 in spermatids. *Dev Cell* **19**:160–173.
720 Kim Y-I, Ryu T, Lee J, Heo Y-S, Ahnn J, Lee S-J, Yoo O. 2010. A genetic screen for modifiers
721 of Drosophila caspase Dcp-1 reveals caspase involvement in autophagy and novel
722 caspase-related genes. *BMC Cell Biol* **11**:9.
723 Liu S-S, Jiang T-X, Bu F, Zhao J-L, Wang G-F, Yang G-H, Kong J-Y, Qie Y-F, Wen P, Fan
724 L-B, Li N-N, Gao N, Qiu X-B. 2024. Molecular mechanisms underlying the BIRC6-
725 mediated regulation of apoptosis and autophagy. *Nat Commun* **15**:891.
726 Muramoto M, Hanawa N, Okumura M, Chihara T, Miura M, Shinoda N. 2025. Executioner
727 caspase is proximal to Fasciclin 3 which facilitates non-lethal activation in Drosophila
728 olfactory receptor neurons. *Elife* **13**:RP99650.
729 Nakajima Y-I, Kuranaga E. 2017. Caspase-dependent non-apoptotic processes in development.
730 *Cell Death Differ* **24**:1422–1430.
731 Nandi N, Tyra LK, Stenesen D, Krämer H. 2014. Acinus integrates AKT1 and subapoptotic
732 caspase activities to regulate basal autophagy. *J Cell Biol* **207**:253–268.
733 Newman BL, Lundblad JR, Chen Y, Smolik SM. 2002. A Drosophila homologue of Sir2
734 modifies position-effect variegation but does not affect life span. *Genetics* **162**:1675–
735 1685.
736 Newton K, Strasser A, Kayagaki N, Dixit VM. 2024. Cell death. *Cell* **187**:235–256.
737 Nezis IP, Shravage BV, Sagona AP, Lamark T, Bjørkøy G, Johansen T, Rusten TE, Brech A,
738 Baehrecke EH, Stenmark H. 2010. Autophagic degradation of dBruce controls DNA
739 fragmentation in nurse cells during late Drosophila melanogaster oogenesis. *J Cell Biol*
740 **190**:523–531.

741 Obata F, Kuranaga E, Tomioka K, Ming M, Takeishi A, Chen C-H, Soga T, Miura M. 2014.
742 Necrosis-driven systemic immune response alters SAM metabolism through the FOXO-
743 GNMT axis. *Cell Rep* **7**:821–833.
744 Okuda S, Watanabe Y, Moriya Y, Kawano S, Yamamoto T, Matsumoto M, Takami T,
745 Kobayashi D, Araki N, Yoshizawa AC, Tabata T, Sugiyama N, Goto S, Ishihama Y.
746 2017. jPOSTrepo: an international standard data repository for proteomes. *Nucleic*
747 *Acids Res* **45**:D1107–D1111.
748 Qin W, Cho KF, Cavanagh PE, Ting AY. 2021. Deciphering molecular interactions by
749 proximity labeling. *Nat Methods* **18**:133–143.
750 Shinoda N, Hanawa N, Chihara T, Koto A, Miura M. 2019. Dronc-independent basal
751 executioner caspase activity sustains Drosophila imaginal tissue growth. *Proc Natl*
752 *Acad Sci U S A* **116**:20539–20544.
753 Shinoda N, Horikoshi M, Taira Y, Muramoto M, Hirayama S, Murata S, Miura M. 2023.
754 Caspase cleaves Drosophila BubR1 to modulate spindle assembly checkpoint function
755 and lifespan of the organism. *FEBS J* **290**:4200–4223.
756 Shinoda N, Miura M. 2024. Exploring caspase-dependent non-lethal cellular processes using
757 Drosophila. *Front Cell Death* **3**:1472108.
758 Taira Y, Yang Z, Miyata Y, Shirasaki Y, Segawa K, Miura M, Shinoda N. 2025. Early-peaking
759 caspase-7 activity at the plasma membrane drives apoptotic phosphatidylserine
760 exposure. *bioRxiv*. doi:10.1101/2025.03.17.643603
761 Tyra LK, Nandi N, Tracy C, Krämer H. 2020. Yorkie growth-promoting activity is limited by
762 Atg1-mediated phosphorylation. *Dev Cell* **52**:605-616.e7.
763 Vaux DL, Silke J. 2005. IAPs, RINGs and ubiquitylation. *Nat Rev Mol Cell Biol* **6**:287–297.
764 Walsh JG, Cullen SP, Sheridan C, Lüthi AU, Gerner C, Martin SJ. 2008. Executioner caspase-
765 3 and caspase-7 are functionally distinct proteases. *Proc Natl Acad Sci U S A*
766 **105**:12815–12819.
767 Wu G, Chai J, Suber TL, Wu JW, Du C, Wang X, Shi Y. 2000. Structural basis of IAP
768 recognition by Smac/DIABLO. *Nature* **408**:1008–1012.
769 Xie HB, Golic KG. 2004. Gene deletions by ends-in targeting in Drosophila melanogaster.
770 *Genetics* **168**:1477–1489.
771 Xu D, Li Y, Arcaro M, Lackey M, Bergmann A. 2005. The CARD-carrying caspase Dronc is
772 essential for most, but not all,developmental cell death in *Drosophila*. *Development*
773 **132**:2125–2134.
774

775 **Figures and figure legends**

776 **Figure 1**

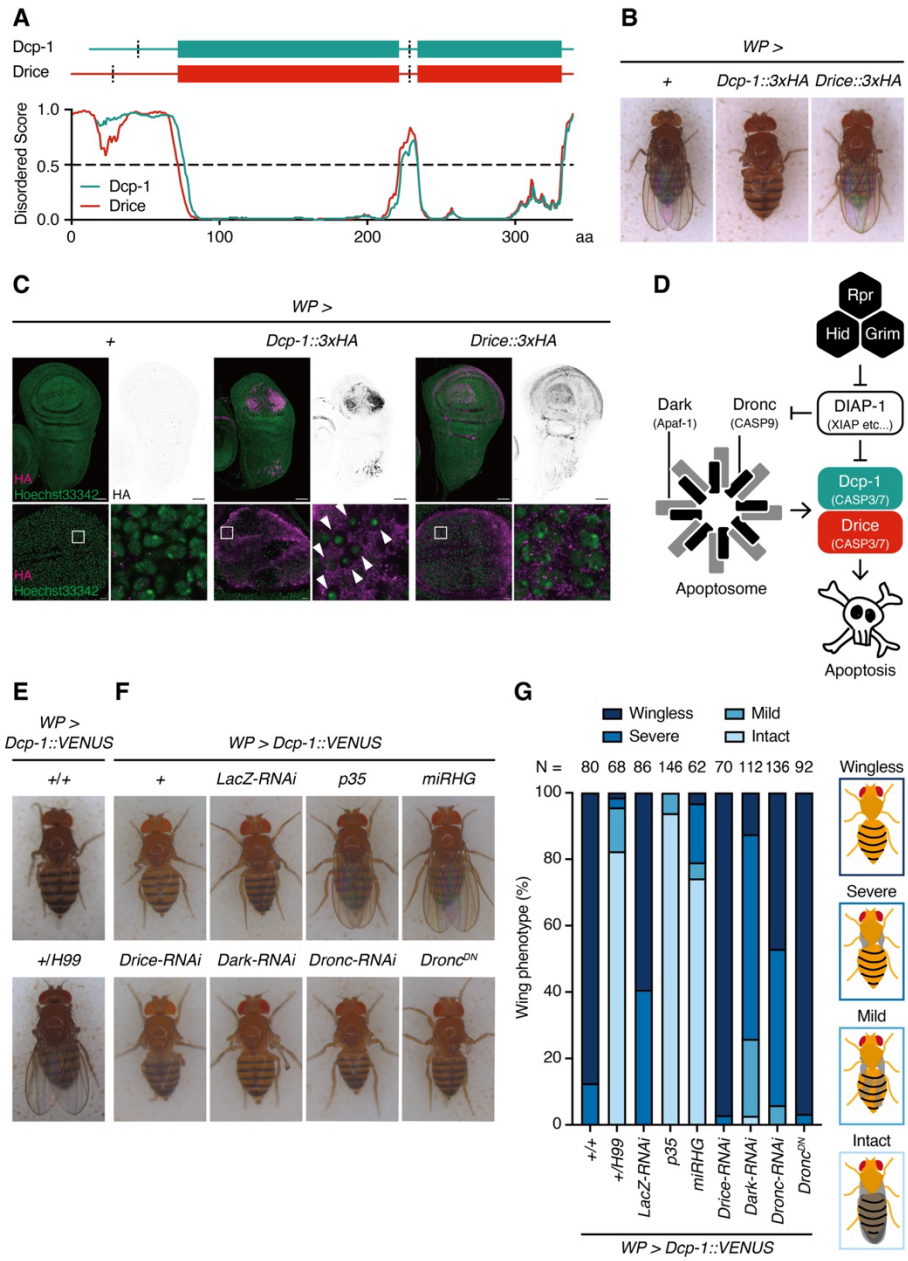

777

778 **Figure 1. *Dcp-1* overexpression induces apoptosis independent of the apoptosome.**

779 (A) Schematic structures and intrinsically disordered region prediction of Dcp-1 (dark cyan)
780 and Drice (red). The predicted disordered score plot is shown. Regions wherein the score is
781 more than 0.5 are predicted to be disordered.

782 (B) Representative images of female wing phenotypes upon caspase overexpression using *WP-*
783 *Gal4*.

784 (C) Representative images of larval wing imaginal disc upon *3xHA-tagged executioner caspase*
785 (magenta) overexpression using *WP-Gal4*. Nuclei are visualized by Hoechst 33342 (green).
786 Magnified images are shown in right below. Arrowheads indicate condensed nuclei. Scale bar:
787 50 µm (top) and 10 µm (bottom).

788 (D) Schematic diagram of canonical apoptosis signaling in *Drosophila*.

(E, F) Representative images of female wing phenotypes upon *Dcp-1::VENUS* overexpression using *WP-Gal4* with the genetic perturbation of canonical apoptosis signaling.
(G) Quantification of (E) and (F). Each wing is manually classified into four (wingless, severe, mild, and intact) categories. Schematic images of the four categories are shown on the right. Sample sizes are shown in the figure.

795 **Figure 1–figure supplement 1**

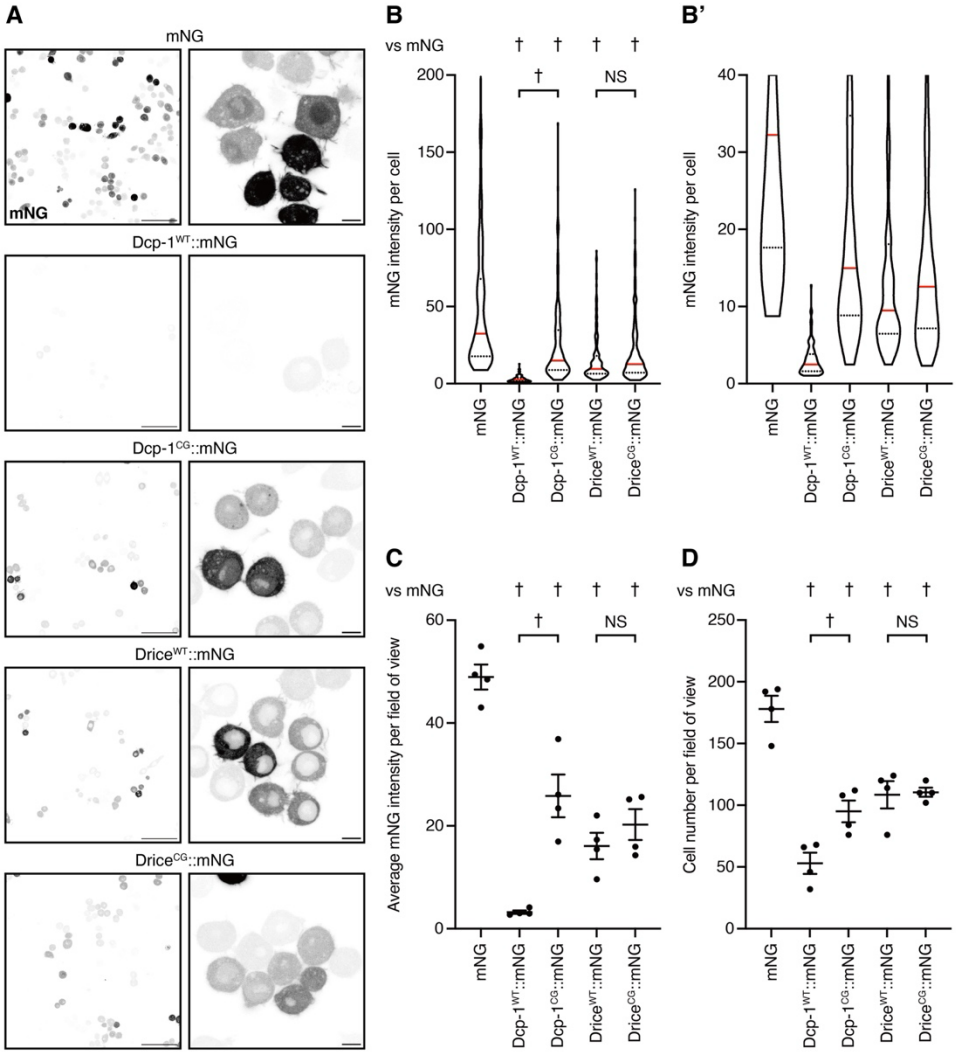

796

797 **Figure 1–figure supplement 1. Dcp-1 overexpression induces apoptosis in *Drosophila* S2**
798 **cells.**

799 (A) Representative images of *Drosophila* S2 cells transfected with mNeonGreen (mNG)-tagged
800 wild-type (WT) or catalytically inactive (catalytic cysteine mutated to glycine; CG) Dcp-1 and
801 Drice. Scale bars: 50 µm (left) and 5 µm (right).
802 (B) Quantification of mNG intensity for each cell, shown as a violin plot. Quartiles are indicated
803 by black broken lines, and the median is indicated by a red bar. (B′) Magnified view of the data
804 in (B), with the Y-axis limited to 0–40. *p*-values were calculated using one-way analysis of
805 variance (ANOVA) followed by Sidak's multiple-comparison test for selected pairs. NS, $p >$
806 0.05; †, $p < 0.05$. Sample sizes: mNG (n = 712 cells), Dcp-1^{WT}::mNG (n = 212 cells), Dcp-
807 1^{CG}::mNG (n = 380 cells), $Drice^{WT}$::mNG (n = 434 cells), and $Drice^{CG}$::mNG (n = 442 cells).
808 (C) Quantification of the average mNG intensity in each field of view. Data are presented as
809 mean ± SEM. *p*-values were calculated using one-way ANOVA followed by Sidak's multiple-
810 comparison test for selected pairs. NS, $p \geqq 0.05$; †, $p < 0.05$. Sample size for each condition is
811 4.

812 (D) Quantification of the mNG-positive cell number in each field of view. Data are presented
813 as mean ± SEM. *p*-values were calculated using one-way ANOVA followed by Sidak's
814 multiple-comparison test for selected pairs. NS, $p \geqq 0.05$; †, $p < 0.05$. Sample size for each
815 condition is 4.
816

817 **Figure 2**

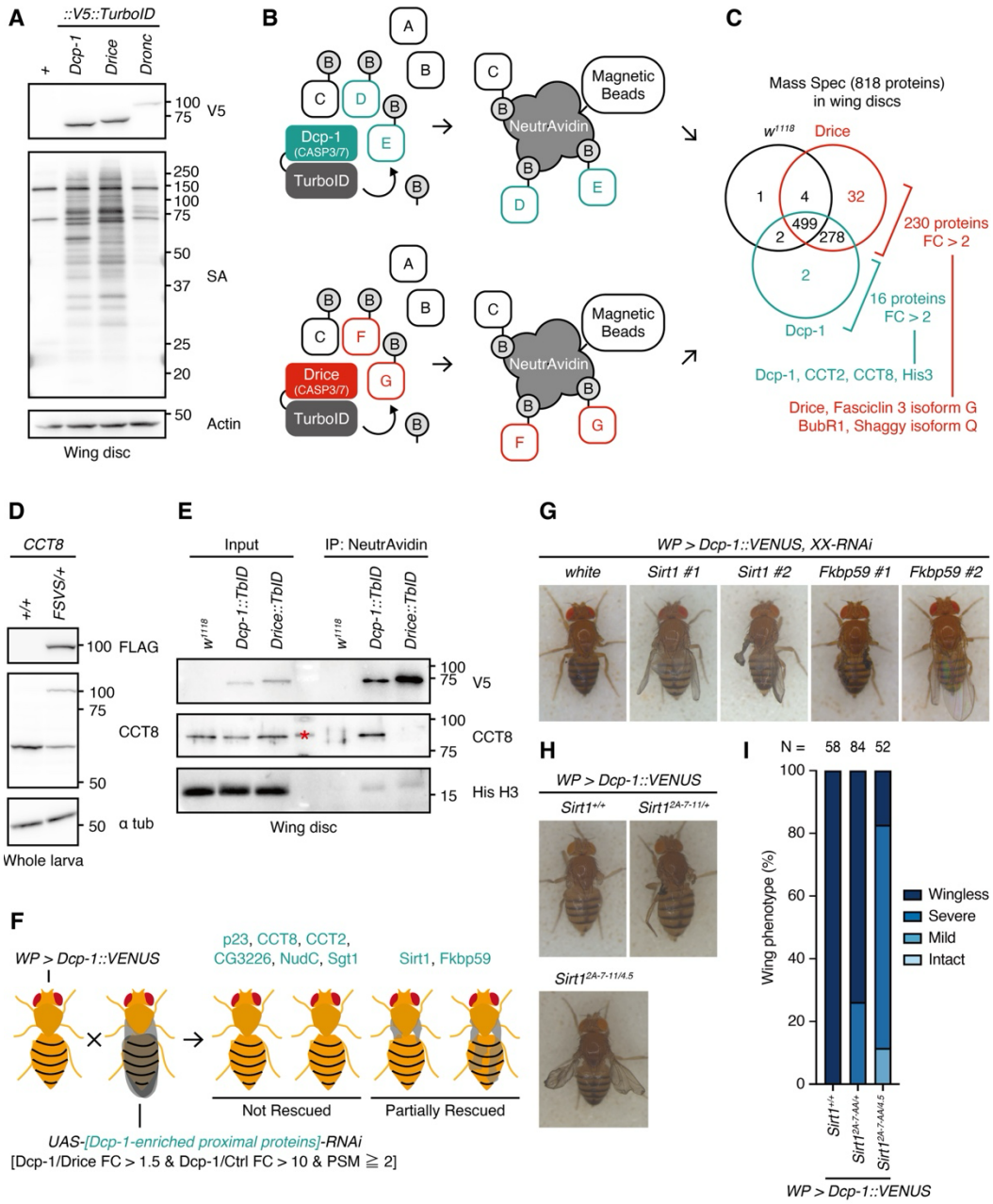

818

819 **Figure 2. Dcp-1-enriched proximal proteins are required for Dcp-1 activation.**

820 (A) Western blotting of expression of C-terminally V5::TurboID knocked-in tagged caspases
821 and biotinylation patterns of their proximal proteins detected by streptavidin (SA) in larval wing
822 imaginal discs.

823 (B) A schematic diagram of the TurboID-mediated identification of proximal proteins. Dcp-1-
824 and Drice-proximal proteins (Protein C, D, E, F, G) are promiscuously labeled in vivo with the
825 administration of biotin. Then, biotinylated proteins are purified using NeutrAvidin magnetic
826 beads and are subsequently analyzed by mass spectrometry.

827 (C) A summary of mass spectrometry analysis of proteins in the larval imaginal discs. Among
828 818 proteins identified, 230 proteins were detected as highly enriched proteins in
829 Drice::V5::TurboID flies (FC [Drice::V5::TurboID/Dcp-1::V5::TurboID] > 2) and 16 proteins

830 were detected as highly enriched proteins in Dcp-1::V5::TurboID flies flies (FC [Dcp-
831 1::V5::TurboID/Drice::V5::TurboID] > 2).
832 (D) Western blotting validation of the anti-CCT8 antibody in whole larval lysates without the
833 digestive tract and fat body. The anti-CCT8 antibody detects both endogenous CCT8 (MW:
834 59.4 kDa) and 3xFLAG::StrepII::VENUS::StrepII (FSVS)-tagged CCT8 (MW: 91.1 kDa).
835 (E) Western blotting of endogenous CCT8 expressed in larval wing imaginal disc. Dcp-1-
836 proximal and Drice-proximal proteins biotinylated by C-terminally knocked-in tagged
837 V5::TurboID are purified using NeutrAvidin. The red asterisk represents a non-specific band
838 in the marker lane.
839 (F) Schematic diagram of the RNAi screen targeting eight Dcp-1-enriched proximal proteins.
840 The *WP > Dcp-1::VENUS* line was crossed with each *UAS-RNAi* line, and wing phenotypes of
841 the F1 progeny were scored.
842 (G) Representative images of female wing phenotypes from *Dcp-1::VENUS* overexpression
843 driven by *WP-Gal4* with knockdown of Dcp-1-enriched proximal proteins. "XX" denotes the
844 knocked-down gene, and "#1" and "#2" indicate independent RNAi lines.
845 (H) Representative images of female wing phenotypes upon *Dcp-1::VENUS* overexpression
846 driven by *WP-Gal4* in the *Sirt1* null mutant background.
847 (I) Quantification of (H). Each wing is manually classified into four (wingless, severe, mild,
848 and intact) categories. Sample sizes are shown in the figure.
849

850 **Figure 2–figure supplement 1**

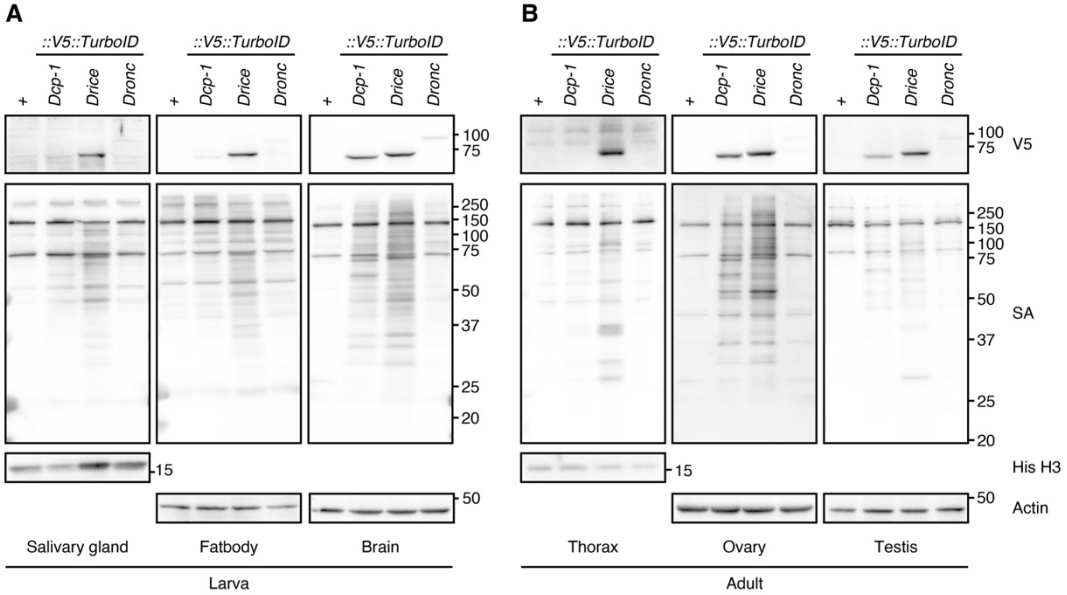

851

852 **Figure 2–figure supplement 1. Expression patterns of *Drosophila* caspases in larval and**

853 **adult tissues.**

854 (A) Western blotting of expression of C-terminally V5::TurboID knocked-in tagged caspases
855 and biotinylation patterns of their proximal proteins detected by streptavidin (SA) in larval
856 salivary gland, fat body, and brain.
857 (B) Western blotting of expression of C-terminally V5::TurboID knocked-in tagged caspases
858 and biotinylation patterns of their proximal proteins detected by SA in adult thorax, ovary, and
859 testis.
860

861 **Figure 2–figure supplement 2**

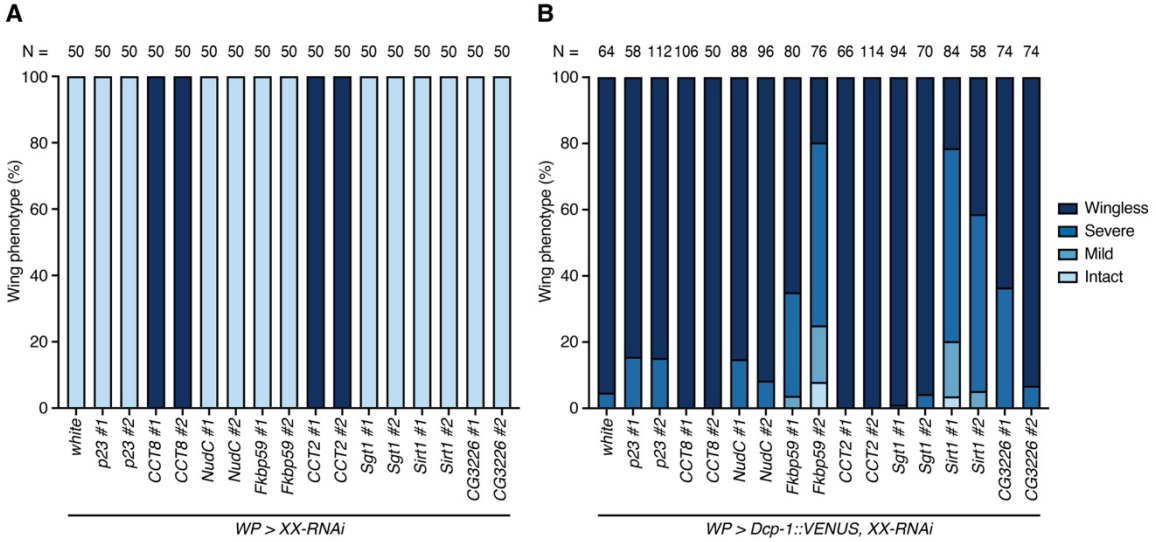

862

863 **Figure 2–figure supplement 2. RNAi screening of Dcp-1-enriched proximal proteins for**

864 **regulators of Dcp-1 activation.**

865 (A) Quantification of female wing phenotypes upon knockdown of Dcp-1-enriched proximal
866 proteins driven by *WP-Gal4*. "XX" denotes the knocked-down gene, and "#1" and "#2" indicate
867 independent RNAi lines. Each wing is manually classified into four (wingless, severe, mild,
868 and intact) categories. Sample sizes are shown in the figure.
869 (B) Quantification of female wing phenotypes upon *Dcp-1::VENUS* overexpression driven by
870 *WP-Gal4* with simultaneous knockdown of Dcp-1-enriched proximal proteins. "XX" denotes
871 the knocked-down gene, and "#1" and "#2" indicate independent RNAi lines. Each wing is
872 manually classified into four (wingless, severe, mild, and intact) categories. Sample sizes are
873 shown in the figure.
874

875 **Figure 3**

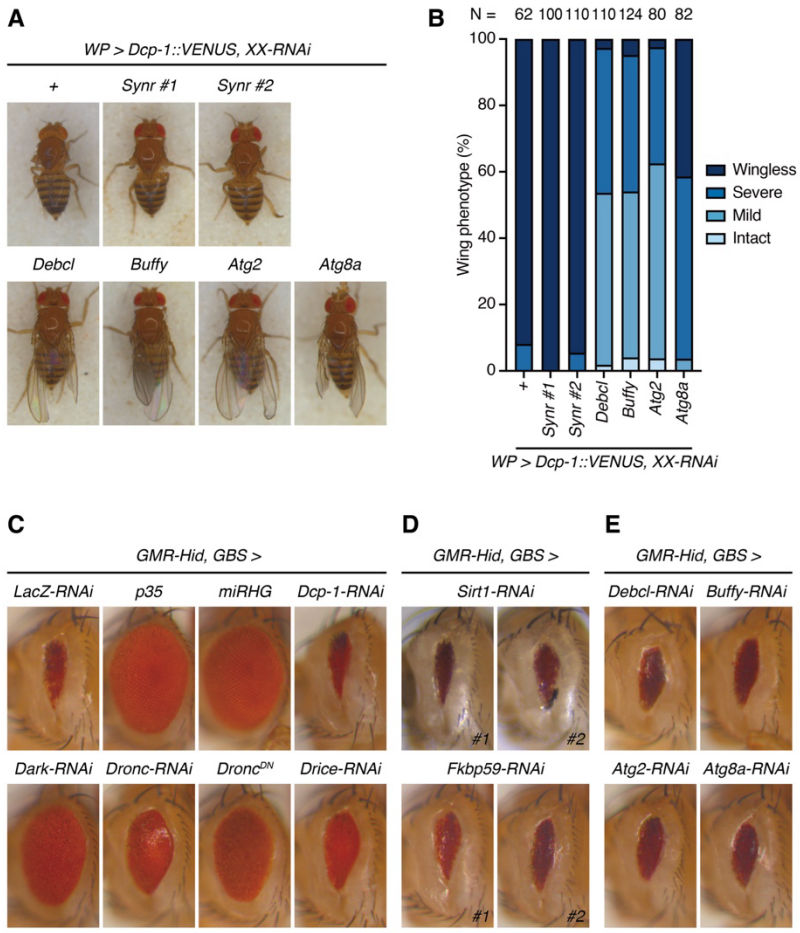

876

877 **Figure 3. Debcl, Buffy, and autophagy are specifically required for *Dcp-1* overexpression-**
878 **induced apoptosis.**

879 (A) Representative images of female wing phenotypes from *Dcp-1::VENUS* overexpression
880 driven by *WP-Gal4* with the genetic perturbation of *Synr*, *Debcl*, *Buffy,* and autophagy. "XX"
881 denotes the knocked-down gene, and "#1" and "#2" indicate independent RNAi lines.

882 (B) Quantification of (A). "XX" denotes the knocked-down gene, and "#1" and "#2" indicate
883 independent RNAi lines. Each wing is manually classified into four (wingless, severe, mild,
884 and intact) categories. Sample sizes are shown in the figure.

885 (C) Representative images of female eye phenotypes upon *Hid* overexpression with the genetic
886 perturbation of canonical apoptosis signaling.

887 (D) Representative images of female eye phenotypes upon *Hid* overexpression with the genetic
888 perturbation of *Sirt1* or *Fkbp59*. "#1" and "#2" indicate independent RNAi lines.

889 (E) Representative images of female eye phenotypes upon *Hid* overexpression with the genetic
890 perturbation of *Debcl*, *Buffy*, and autophagy.

891

892 **Figure 4**

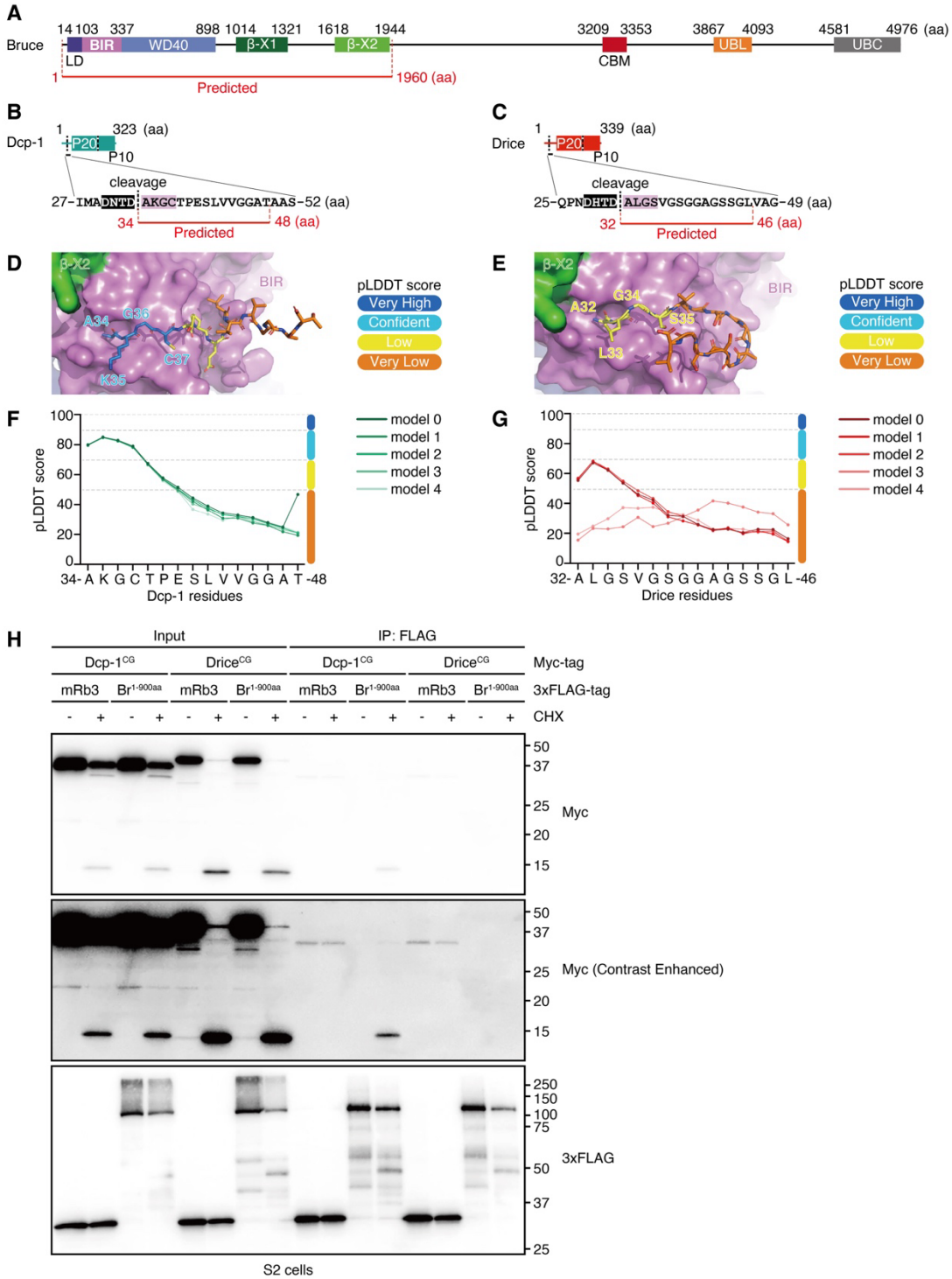

893

894 **Figure 4. Cleaved Dcp-1, but not Drice, interacts with Bruce.**

895 (A) Domain structure of Bruce. LD denotes the linker domain, WD40 a WD40 domain, BIR
896 the Baculoviral IAP repeat, β-X a β-sandwich-like fold, CBM a domain resembling the
897 carbohydrate-binding module family 32 (CBM), UBL the ubiquitin-like domain, and UBC the
898 E2-E3 hybrid ubiquitin-conjugating (UBC) domain. The region used for structural prediction
899 using AlphaFold3 is indicated in red.

(B) IBM-like sequence in Dcp-1. The propeptide cleavage site of Dcp-1 is indicated by a black dashed line; the caspase recognition motif is highlighted in black; the IBM-like sequence is highlighted in pink; and the region used for AlphaFold3 prediction is shown in red.
(C) IBM-like sequence in Drice. The propeptide cleavage site of Drice is indicated by a black dashed line; the caspase recognition motif is highlighted in black; the IBM-like sequence is highlighted in pink; and the region used for AlphaFold3 prediction is shown in red.
(D) Predicted complex structure of Bruce BIR and Dcp-1 IBM-like sequence. The AlphaFold3 prediction [model 0] is shown. The Bruce β-X2 and BIR domains are displayed as surfaces in green and pink, respectively. Dcp-1 is shown in stick representation and color-coded according to pLDDT scores, as indicated in the figure. See also panel (F).
(E) Predicted complex structure of Bruce BIR and Drice IBM-like sequence. The AlphaFold3 prediction [model 0] is shown. The Bruce β-X2 and BIR domains are displayed as surfaces in green and pink, respectively. Drice is shown in stick representation and color-coded according to pLDDT scores, as indicated in the figure. See also panel (G).
(F) pLDDT scores of Dcp-1 in the five predicted complex structures with Bruce. For all five AlphaFold3 models, per-residue pLDDT scores of Dcp-1 are plotted. Prediction confidence is color-coded as follows: very high (pLDDT > 90) in dark blue, confident (90 > pLDDT > 70) in light blue, low (70 > pLDDT > 50) in yellow, and very low (pLDDT < 50) in orange.
(G) pLDDT scores of Drice in the five predicted complex structures with dBruce. For all five AlphaFold3 models, per-residue pLDDT scores of Drice are plotted. Prediction confidence is color-coded as follows: very high (pLDDT > 90) in dark blue, confident (90 > pLDDT > 70) in light blue, low (70 > pLDDT > 50) in yellow, and very low (pLDDT < 50) in orange.
(H) Co-immunoprecipitation of N-terminally 3xFLAG-tagged N-terminal region of Bruce (Br, 1–900 aa; containing LD, BIR, and WD40 domains) with C-terminally myc-tagged, catalytically inactive Dcp-1 or Drice (catalytic cysteine mutated to glycine; CG) expressed in *Drosophila* S2 cells. N-terminally 3xFLAG-tagged mRuby3 (mRb3) was used as a control. Apoptosis was induced by cycloheximide (CHX) treatment. 3xFLAG-tagged proteins were immunoprecipitated using an anti-3xFLAG antibody.

929 **Figure 4–figure supplement 1**

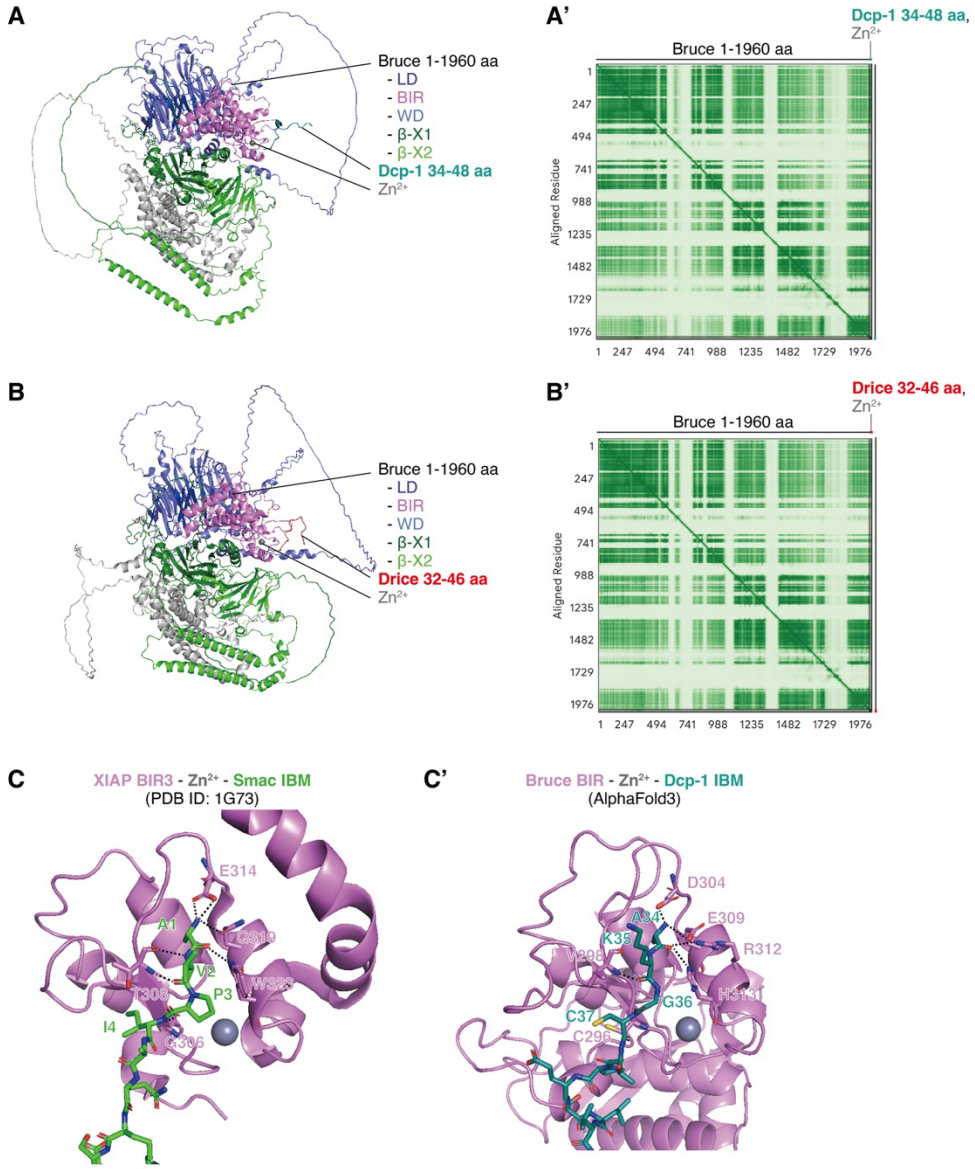

930

931 **Figure 4–figure supplement 1. Predicted structures of Bruce complexed with Dcp-1 and**
932 **Drice IBM-like sequences.**

933 (A) Overall view of the predicted complex structure of Bruce and Dcp-1. Model 0 is shown
934 with the same color scheme as in Figure 4A and B. The predicted position error is shown in
935 (A').
936 (B) Overall view of the predicted complex structure of Bruce and Drice. Model 0 is shown with
937 the same color scheme as in Fig. 4A and C. The predicted position error is shown in (B').
938 (C) Structural comparison between the experimentally determined complex of XIAP BIR3 and
939 Smac IBM (C), and the predicted complex of dBruce BIR and Dcp-1 IBM (C'). XIAP BIR3 is
940 shown as a pink cartoon and the Smac IBM as green sticks (PDB ID: 1G73, right panel). dBruce
941 BIR domain is shown as a pink cartoon and the Dcp-1 IBM as dark green sticks (model 0, left
942 panel). Zn^{2+} ions are shown as gray spheres. Salt bridges are indicated by black dashed lines,
943 along with the corresponding interacting residues.

944 **Figure 5**

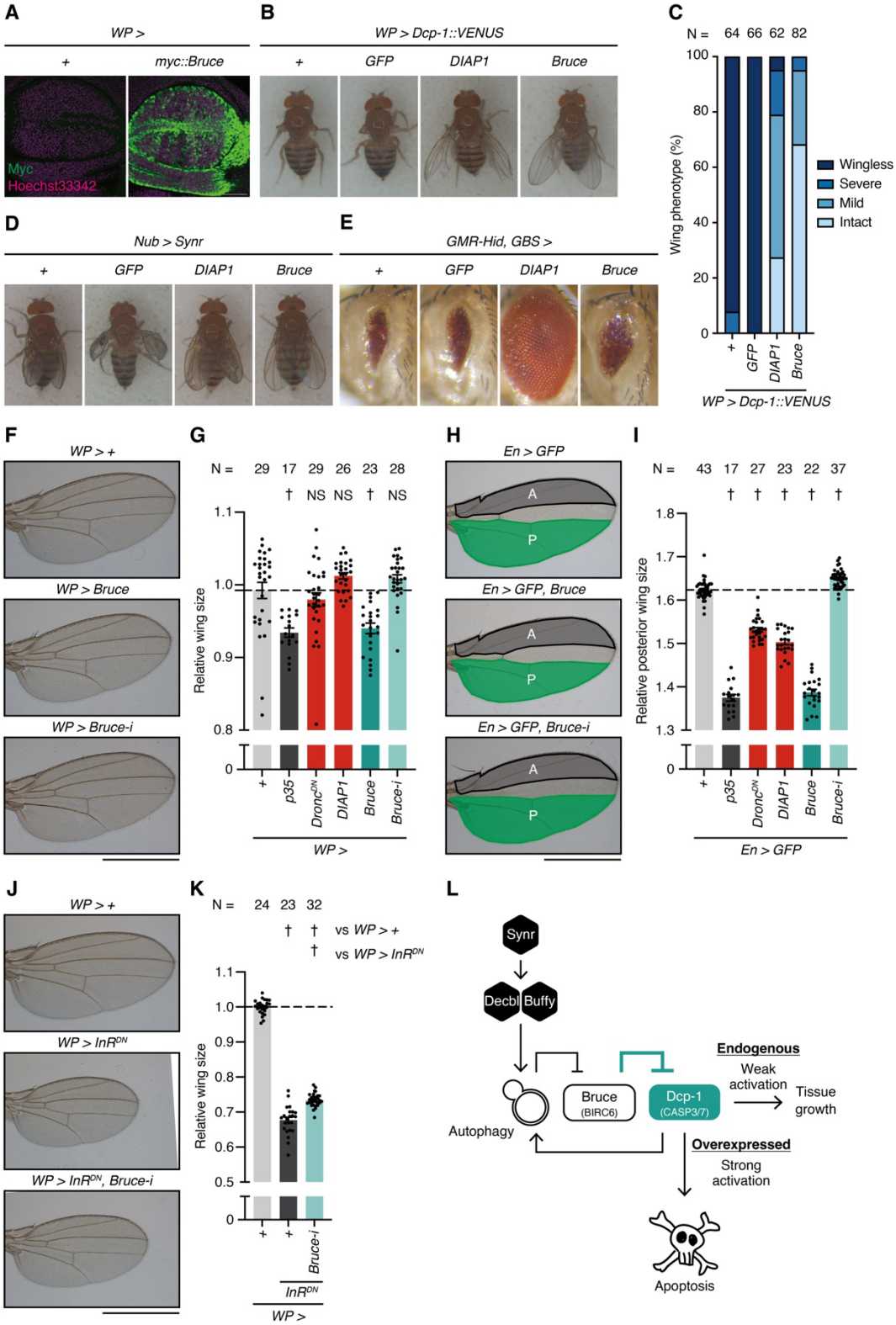

945

946 **Figure 5. Bruce selectively suppresses Dcp-1 activity and wing tissue growth.**

947 (A) Expression pattern of overexpressed *myc::Bruce* (green) by using *WP-Gal4* in the wing

948 imaginal discs. Nuclei are visualized using Hoechst 33342 (magenta). Scale bar: 50 µm.

(B) Representative images of female wing phenotypes from *Dcp-1::VENUS* overexpression driven by *WP-Gal4* with *DIAP1* or *Bruce* overexpression.
(C) Quantification of (B). Each wing is manually classified into four (wingless, severe, mild, and intact) categories. Sample sizes are shown in the figure.
(D) Representative images of female wing phenotypes upon *Synr* overexpression driven by *Nub-Gal4* with *DIAP1* or *Bruce* overexpression.
(E) Representative images of female eye phenotypes upon *Hid* overexpression with *DIAP1* or *Bruce* overexpression.
(F) Representative images of female wing upon *Bruce* or *Bruce-RNAi* (*Bruce-i*) overexpression using *WP-Gal4*. Scale bar: 1 mm.
(G) Quantification of relative wing size normalized to the corresponding *No-Gal4* control. Data are presented as mean ± SEM. *p*-values were calculated using one-way analysis of variance (ANOVA) followed by Dunnett's multiple-comparison test against no UAS control. NS, $p \geqq 0.05$; †, $p < 0.05$. Sample sizes are shown in the figure.
(H) Representative images of female wing upon *Bruce* or *Bruce-RNAi* (*Bruce-i*) overexpression using *En-Gal4*. The grey area (labelled as A) represents the anterior part, and the green area (labelled as P) represents the posterior part of the wing. Scale bar: 1 mm.
(I) Quantification of relative posterior part of wing size normalized to corresponding anterior part of wing size. Data are presented as mean ± SEM. *p*-values were calculated using one-way ANOVA followed by Dunnett's multiple comparison test against no UAS control. †, $p < 0.05$. Sample sizes are shown in the figure.
(J) Representative images of female wing upon InR^{DN} and *Bruce-RNAi* (*Bruce-i*) overexpression using *WP-Gal4*. Scale bar: 1 mm.
(K) Quantification of relative wing size normalized to control (*WP* > +). Data are presented as mean ± SEM. p-values were calculated using one-way ANOVA followed by Sidak's multiple comparison test for selected pairs.†, $p < 0.05$. Sample sizes are shown in the figure.
(L) Schematic diagram of Dcp-1 activity-regulating alternative apoptosis signaling pathway in *Drosophila* mediated by autophagy-Bruce axis.

978 **Figure 5–figure supplement 1**

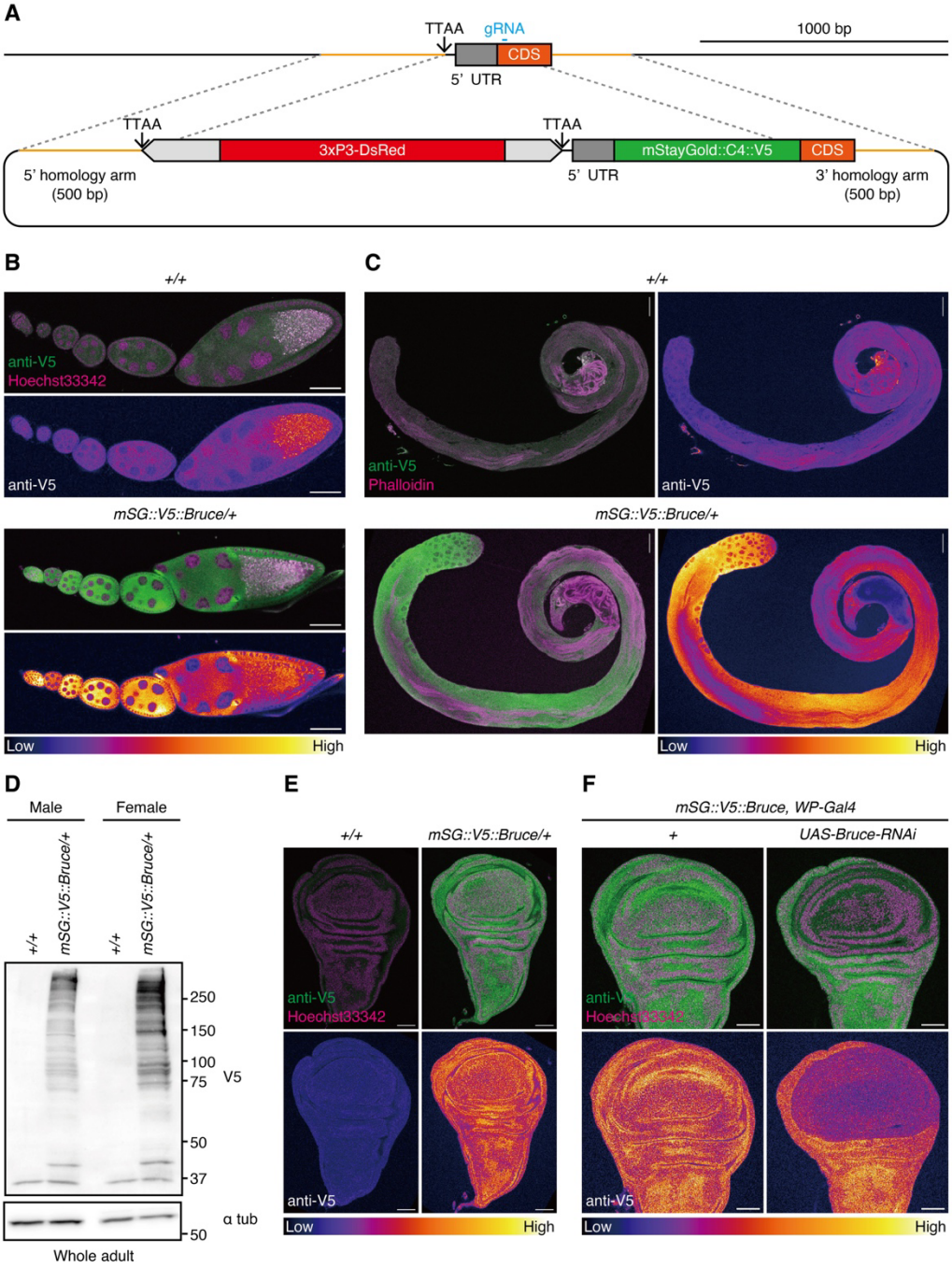

979

980 **Figure 5–figure supplement 1. Expression patterns of mStayGold::V5-tag knocked-in**

981 **Bruce.**

982 (A) Schematic diagram of CRISPR/Cas9-mediated knock-in of mStayGold::C4 linker (C4)::V5
983 tag at the N-terminus of Bruce. A 3xP3-DsRed cassette was integrated at the endogenous TTAA
984 site as a transformation marker. Removal of the cassette restores the genomic TTAA site,
985 enabling scarless genome engineering.
986 (B) Expression pattern of mStayGold (mSG)::C4::V5-tag knocked-in Bruce (green) in the
987 ovariole. Nuclei are visualized using Hoechst 33342 (magenta). Scale bar: 50 μm.

988 (C) Expression pattern of mSG::C4::V5-tag knocked-in Bruce (green) in the testis. Nuclei are
989 visualized using Hoechst 33342 (magenta). Scale bar: 50 µm.
990 (D) Western blotting of expression of mSG::C4::V5-tag knocked-in tagged Bruce in the whole
991 adult male and female.
992 (E) Expression pattern of mSG::C4::V5-tag knocked-in tagged Bruce (green) in the wing
993 imaginal discs. Nuclei are visualized using Hoechst 33342 (magenta). Scale bar: 50 µm.
994 (F) Expression pattern of mSG::C4::V5-tag knocked-in tagged Bruce (green) in the wing
995 imaginal discs upon *Bruce-RNAi* using *WP-Gal4*. Nuclei are visualized using Hoechst 33342
996 (magenta). Scale bar: 50 µm.
997

998 **Legends for Supplemental Tables**
999
1000 **Table S1. Dcp-1 and Drice proximal protein lists.**
1001 Lists of the identified Dcp-1 proximal proteins (abundance ratio (Dcp-
1002 1::V5::TurboID/Drice::V5::TurboID) > 2), Drice proximal proteins (abundance ratio
1003 (Drice::V5::TurboID/Dcp-1::V5::TurboID) > 2), and candidates for RNAi screening
1004 (abundance ratio (Dcp-1::V5::TurboID/Drice::V5::TurboID) > 1.5, abundance ratio (Dcp-
1005 1::V5::TurboID/Control) > 10, PSM ≧ 2). The UniProt accessions, gene description,
1006 abundance ratio, and # PSMs are listed.
1007
1008 **Table S2. Fly stock list.**
1009 List of fly strains. Genotypes, maps, source or references, and stock numbers are listed.
1010
1011 **Table S3. Detailed genotypes.**
1012 Detailed genotypes and their related figure # are presented.
1013
1014 **Table S4. Liquid chromatography (LC) settings.**
1015 Gradient settings for LC analysis are presented.
1016
1017 **Table S5. Tandem mass spectrometry (MS/MS) settings.**
1018 Settings used for the MS/MS analysis are presented.
1019
1020 **Table S6. Proteome Discoverer 2.2 settings.**
1021 Proteome Discoverer 2.2 settings for proteomics analysis are presented.
1022